UPPSALA
UNIVERSITET

UPTEC STS 20036
Examensarbete 30 hp
December 2020

Temperature Dependence of Resistance of a Ni-rich Li-ion Cathode

UPPSALA
UNIVERSITET

Teknisk- naturvetenskaplig fakultet
UTH-enheten

Besöksadress:
Ångströmlaboratoriet
Lägerhyddsvägen 1
Hus 4, Plan 0

Postadress:
Box 536
751 21 Uppsala

Telefon:
018 – 471 30 03

Telefax:
018 – 471 30 00

Hemsida:
http://www.teknat.uu.se/student

Abstract

Temperature Dependence of Resistances of a Ni-rich Li-ion Cathode

Ewa Töyrä Mendez

Understanding the degradation mechanisms of Li-ion batteries is essential to gain insights into battery aging. The primary research area of this thesis is the positive electrode, NMC811. The purpose of the thesis is to understand how low and elevated temperatures affect the aging of NMC811, by considering the effects on resistance. The aim of the thesis is to investigate the degradation mechanisms of NMC811. Here, three electrode Li-ion pouch cells are assembled with LiNi8Mn1Co1O2 (NMC811) as the positive electrode, graphite as the negative, gold wire as the reference electrode, and LiPF6 as the electrolyte. The positive electrode impedance is recorded at temperatures –10, 22, and 40 °C. Also, symmetric and half cells are built for validation measurements. The Nyquist diagrams are fitted through equivalent circuits to determine the cells' impedance at voltages 3.8 and 3.0 V vs Li+/Li. The resistances observed and analyzed in this project are the high-frequency resistance, the contact resistance, the charge transfer resistance, and the resistance due to the electrode–electrolyte interphase. By comparing these resistances, it is observed that the charge transfer resistance has the highest dependence on the ambient temperature. The increase in charge transfer resistance at –10 °C is suggested to depend on the Ni-rich electrode, which tends to contribute to volume changes in the electrode, affecting the intercalation and de-intercalation of Li-ions. The resistance reduces significantly at 40 °C, due to the loss of lithium inventory in the active material. This thesis has thus shown that temperature has a significant effect on cell internal resistance, especially on the electrode–electrolyte interface, which describes the charge transfer reactions.

Handledare: Erik Berg
Ämnesgranskare: Jonas Mindemark
Examinator: Elisabet Andrésdóttir
ISSN: 1650-8319, UPTEC STS 20036

Acknowledgements

This degree project comprises 30 hp and completes the master's degree program in sociotechnical systems engineering at Uppsala University. The supervisors for this thesis have been Erik Berg and Anastasiia Mikheenkova, at the Department of Structural Chemistry – Ångström Laboratory. Jonas Mindemark at the Department of Chemistry – Ångström Laboratory, has been my subject reviewer for this project.

I would like to express my gratitude to the people who have supervised me during my thesis. Thank you Erik for allowing me to do my thesis at one of the best battery labs in the world, taking on the supervisor assignment, and pedagogically shared your expertise in the subject. Thank you Anastassiia for guiding me through the project, being an inspirational role model, and for making chemistry fun. You have taught me an incredible amount. Thank you Jonas for your commitment, knowledge, and support during the work. Thank you all for your valuable time, knowledge, and help.

I would also like to thank my family and friends for the support. A special thanks to my grandma Ewa Töyrä, my mother Cecilia Mendez, and my little brother Sebastian Töyrä Mendez for always believing in me throughout my years of studies.

Ewa Töyrä Mendez

Uppsala, november 2020

Populärvetenskaplig sammanfattning

Transportsektorn står idag för cirka en fjärdedel av Europas utsläpp av växthusgaser och är enligt europeiska kommissionen definierad som den främsta orsaken till luftföroreningar i städer. För att uppnå europeiska kommissionens klimatmål 2030 måste växthusgasutsläppen minska med minst 40%, jämfört med nivåerna från 1990. En strategi för att möta detta mål är att påskynda utvecklingen av utsläppsfria fordon, såsom elfordon. Idag är litiumbatteriet ett av de mest tillämpade batterierna i elfordon, då den bland annat har förmågan att leverera hög effekt. Litiumbatteriet saknar dock förmågan att möta flera av de utmaningar som elbilar ställs inför dagligen, såsom omgivningsförhållanden som blandat påverkas av temperaturvariationer och dynamisk användning. Idag ligger de optimala driftstemperaturerna för de vanligaste litiumbatterier på mellan 15 till 40 ºC, men det finns en stor marknadsefterfrågan på litiumbatterier som tål temperaturer på minst 60 ºC. Detta är dock bortom dagens befintliga teknik för en del typer av litiumbatterier. Nuvarande publikationer har antytt vikten av att studera degrationsprocessena i litiumbatterier för att få kunskap om vad som bidrar till litiumbatteriers åldrande.

En battericell består av fyra funktionella komponenter; en positiv och en negativ elektrod, separerade med en jonledare, kallad elektrolyt, samt en porös separator. Dessutom består en battericell också av strömledare som möjliggör transporten av elektroner mellan den positiva och negativa elektroden. Idag pågår det forskning och utveckling kring olika uppsättningar av litiumbatterier som bland annat kan maximera batteriernas livslängd, säkerhet, uppladdningshastighet, samt minimera kostnader och underhåll. Den här rapporten ämnar att undersöka den nickelrika katoden NMCs temperaturberoende, i form att resistanspåverkan. Syftet med rapporten är att förstå hur höga och låga temperatur påverkar degrationsprocesserna av NMC, ett ämne som brukar förknippas med batteriåldring. Det aktiva materialet i den positiva elektroden består av litium, nickel och mangankoboltoxid, och har uppmärksammats på grund av dess lovande kemiska egenskaper, som bland annat bidrar till höga spänningar. Temperatureffekten på degrationsprocesserna i NMC undersöks på temperaturerna –10, 22 och 40 ºC. I den här rapporten har litiumceller bestående av NMC som positiv elektrod, grafit som negativ elektrod, och guld som referenselektrod, konstruerats för att laddas upp och ur vid de tre olika temperaturerna. Impedansmätningar har sedan uppmätts på spänningarna 3.0 och 3.8 V vs. Li^+/Li.

Resultaten visar att temperaturerna 40 och –10 ºC, haft en betydande inverkan på NMC cellens interna resistanser. Projektet har konstaterat att nickelrika elektroder tenderar att bidra till volymändringar i elektroden, vilket påverkar överföringen av litiumjoner mellan elektroderna, och även till en högre cellimpedans vid –10 ºC. Vid 40 ºC ökar impedansen av cellen på grund av förlusten av litium i den positiva elektroden.

Table of Contents

Abbreviations

AC	Alternating Current
C-rate	Current Rate
CC	Current Collector
CEI	Cathode Electrode Interphase
CPE	Constant Phase Element
DC	Direct Current
DX	Extended Element
EIS	Electrochemical Impedance Spectroscopy
EV	Electric Vehicle
GWRE	Golden Wire Reference Electrode
HFR	High Frequency Region
LCO	Lithium Cobalt Oxide
LFP	Lithium Iron Phosphate
LIB	Lithium-Ion Battery
LMO	Lithium Manganese Spinel
NMC	Nickel Manganese Cobalt
R	Resistor
TLM	Transmission Line Model
SEI	Solid Electrolyte Interphase
SoC	State of Charge
W	Warburg Element

1. Introduction

In order to meet the European Commission's climate target by 2030, the greenhouse gas emissions must be reduced by at least 40 %, compared to the levels from 1990.[1] The transportation sector stands today for about a quarter of Europe's greenhouse gas emissions and is according to the European Commission defined as the main cause of air pollution in cities.[2] To face this target, the strategy to speed up the development of low-emission alternatives for the transportation sector has been specified as a priority action, as well as moving towards zero-emission vehicles.[2] Electric vehicles, EVs, have therefore been addressed as sustainable solutions to replace the combustion engine. There are, however, several concerns associated with the development of the batteries used in EVs, such as cycle life, safety, and capacity. Currently, numerous different rechargeable battery chemistries are used in EV applications, with the intention to hold high energy density, low cost and maintenance, high charging and discharging rate, long lifetime, and high stability.[3]

One of today's most widely used rechargeable batteries is the lithium-ion battery, LIB. Its popular features for the EV industry are its ability to deliver high power and hold high energy densities.[4] The favorable properties are due to Li being the lightest of metals, with a low electrochemical potential of –3.04 V vs. Li^+/Li. Furthermore, the LIB cells allow for fast charging and an acceptable long shelf-life.[5] The most commonly used anode material in LIBs is graphite, mainly due to its low potential, its high specific capacity of 372 mAh/g, and its ability to reversibly insert and extract a large amount of Li-ions.[6] Today's LIBs are well suitable for plug-in hybrid electric vehicles but do still lack in meeting the challenges that EVs provide, such as operating under varying ambient conditions, such as during temperature variations.[3] LIBs are electrochemical systems, in which unwanted side reactions in the battery lead to capacity fade over time and to an increase in resistance, resulting in the aging of the battery.[7] Present publications have implied the importance of studying the aging mechanisms of full cell cycling to gain knowledge about cell degradation, and further, why cells do fail.[8] A major consideration as to why it is important to minimize the rise of cell resistance, an effect of cell aging, is due to the fact that an increase in resistance results in a decrease of attainable power and a decrease in capacity.[4]

The performance of an electrochemical cell is highly dependent on the operational temperature, which in turn affects many other parameters, such as resistance, and in turn battery lifetime.[6] Today, the optimal operating temperatures for LIBs range between 15 and 40 °C. Once the LIB operates outside this range, the possibility of rapid cell aging increases and the battery degrades fast, resulting in a shorter lifetime.[9] It is therefore important to understand how LIB materials are affected by temperature, in order to use the battery most optimally, securing performance, safety and lifetime.[6]

Furthermore, LIBs are named according to their cathode (positive electrode) materials.[3] The most leading technologies for EVs are lithium nickel manganese cobalt oxide (NMC), lithium manganese spinel (LMO), and lithium iron phosphate (LFP). The LFP battery allows for high usable capacity and is the safest Li-ion battery, due to its stable chemistry. NMC is possibly the most common battery used in EVs as it has stable chemistry, relatively low costs, and consists of only a relative small portion of cobalt, a component associated with extraction complications.[10] Further, NMC allows fast-charging and provides high energy density.[11] LMO-batteries allow for acceptable safety performance and low costs, in comparison to Ni- and Co-based oxide materials. However, due to their short lifecycle, the durability of the battery is not long, especially not at elevated temperatures.[12] Furthermore, lithium cobalt oxide (LCO) is one of the most common positive electrode materials used in portable devices. The major disadvantages with the material are, however, its high costs due to the use of cobalt and its poor thermal stability.

In this project, the NMC811 positive electrode is of interest. NMC811 refers to its transition metal composition of 80 % nickel, 10 % manganese and 10 % cobalt, together with lithium and oxygen, making lithium nickel manganese cobalt oxide, $Li(Ni_{0.8}Mn_{0.1}Co_{0.1})O_2$. In comparison to LCO, NMC811 has lower costs, long cycle life, high energy density and good thermal stability.[13]

1.1 Scope of the Thesis

Within this thesis, the emergence of cell resistance in the full cell battery is examined. This project focuses mainly on the positive electrode, with NMC811 as the primary research area. The negative electrode is composed of graphite. The purpose of the project is to develop an understanding of how temperature rise and fall affect the aging of NMC811, by the development of equivalent circuit models, which describe the effects of temperature on impedance. The impedance effect is investigated at temperatures –10, 22 and 40 ºC, during cycling. This project aims to investigate the degradation of the positive electrode, with NMC811 as active material, a matter referred to as battery aging. Furthermore, it aims to explain how and why an increase and decrease in ambient temperature affects the resistance in this type of battery cell.

2. Background

EVs require a dynamic usage of their battery, often demanding high currents of charge and discharge which arise in the driving patterns of acceleration and breaking. These dynamics, in combination with ambient temperature variations, affect the battery's performance and durability. In terms of these demands, the LIB technology is currently the most suitable technology, combining high energy densities and high power capabilities.[14] Batteries do, however, show performance losses during their lifetime associated with a decrease in capacity and increase in resistance, leading to loss of power. The degradation factors causing these performance losses arise from the usage and cell design of the battery.[15] The cause of capacity fade and resistance increase is specific to each battery chemistry and affects the battery's degradation performance.[4]

2.1 The Li-Ion Battery

A battery is an electrochemical cell that acts as a galvanic cell when converting chemical energy to electrical energy during discharge, and as an electrolytic cell when electrical energy is converted to chemical energy during charging.[6] Within a battery there exist one or several cell units, in which the electrochemical cell is the smallest unit that converts chemical energy to electrical energy, and vice versa.[16] A battery cell consists of four functional components; a positive and a negative electrode, separated by an ionic conductor called electrolyte and a porous separator. Furthermore, it also consists of current collectors, which allow the transportation of electrons between the positive and negative electrodes. Specifically, for LIBs, the positive electrode generally consists of a mixture containing active material, conductive additives (materials used to enhance electric conductivity) and binder, coated onto the metallic current collector. The negative electrode commonly consists of a mixture of graphite and binder coated onto another metallic current collector. When charging or discharging a cell, mobile ions are inserted/extracted into/from the active sites in the active material through electrochemical reactions.[4] Figure 1 shows the transportation of Li-ions during charging and discharging.

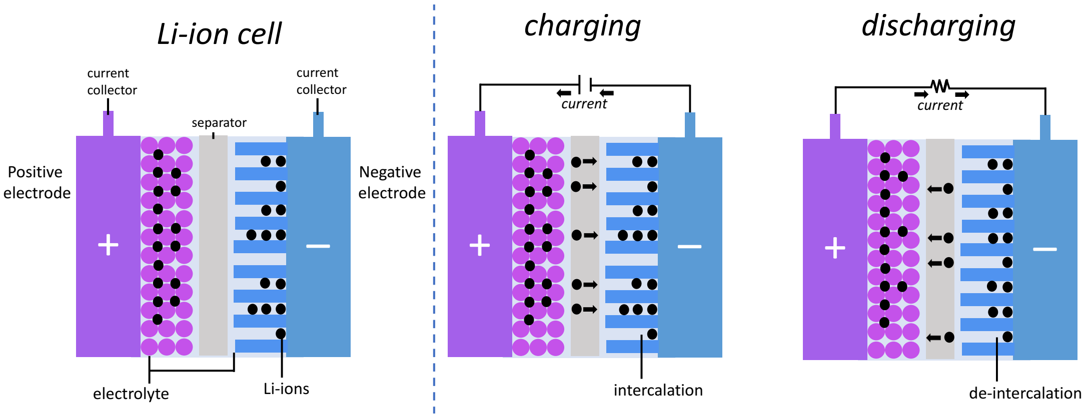

Figure 1. Li-ions movement in electrolyte and intercalation/de-intercalation within electrodes in a LIB.

The main function of the electrolyte is to allow the transfer of ions and not electrons. The electrolyte must be compatible with the electrodes used, without failing in performance, and while still being stable within the full voltage range of the cell.[6] The separator is placed in between the positive and negative electrodes, preventing electrical contact of the electrodes while enabling ionic transport.[4] Requirements for the separator are to be a porous membrane soaked in the electrolyte solution, allowing ion transfer and preserving the electronic insulating properties.[6]

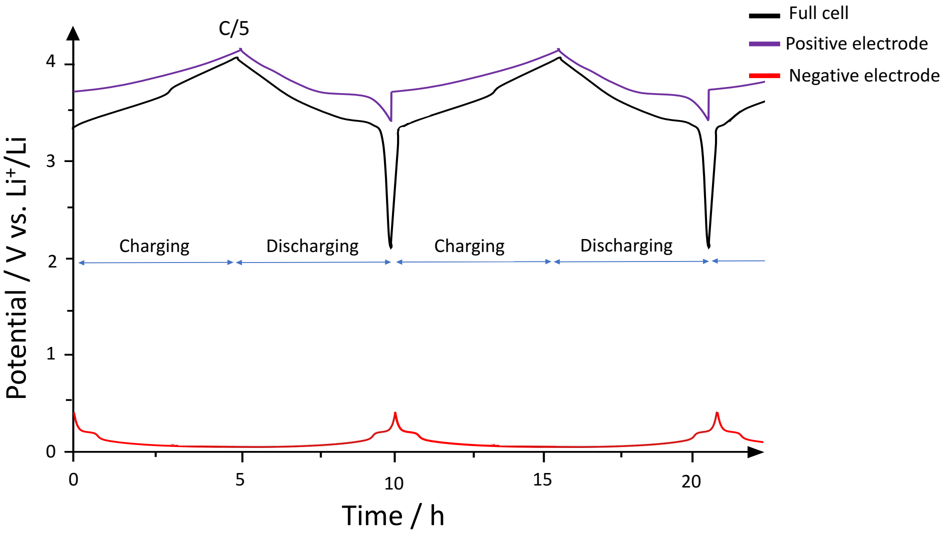

Figure 2. The voltage of the full cell. The electrode potentials are usually measured against Li metal as it is considered to have a potential of 0 V vs. Li^+/Li.

During discharge, an oxidation reaction occurs at the negative electrode, simultaneously as a reduction reaction happens at the positive electrode. Li-ions are transported from the negative electrode to the positive electrode, across the electrolyte and intercalated at the surface of the positive electrode. As a result, charge-compensating electrons flow through the external load to close the circuit. The same but opposite principle occurs in the cell during charging.[4] During cell cycling, a charge transfer reaction occurs at the interfaces of the electrodes and the electrolyte, in which Li-ions are intercalated or de-intercalated in the electrodes and electrons are transported between the electrodes.[17] The full potential of a battery is defined as the difference between the potential of the positive and negative electrode, as displayed in Figure 2. The figure also includes a C-rate of C/5, which describes the cell's charging time, also called the current rate. The rate at which the Li-ions are transferred from one electrode to another impacts the performance of the battery. The charge reactions, also called redox reactions, at the negative and positive electrodes, considering a graphite-based negative electrode and a Li-based positive electrode, can be written as (1) and (2). Here, the variable x represents the mole quantity and M refers to the transition metal.[4]

$$\text{Positive electrode: } x\mathrm{Li}^{+} + x\mathrm{e}^{-} + x\mathrm{C}_6 \rightarrow x\mathrm{LiC}_6 \tag{1}$$

$$\text{Negative electrode: } \mathrm{Li}M\mathrm{O}_2 \rightarrow x\mathrm{Li}^{+} + x\mathrm{e}^{-} + \mathrm{Li}_{1-x}M\mathrm{O}_2 \tag{2}$$

Equations (1) and (2) illustrate, during charging, the negative electrode active material is intercalated with Li-ions, while the positive electrode active material is de-intercalated. During discharging, the direction of the process is reversed.[4]

2.2 Lithium Nickel Manganese Cobalt Oxide and Graphite

The active material in the positive electrode consists of lithium nickel manganese cobalt oxide and has received attention due to its promising electrochemical properties, performance and thermal stability.[18] NMC is referred to as one of the high-voltage electrode materials. Compared to other conventional positive electrode materials, NMC succeeds in achieving high discharge voltages, up to 5 V vs. $\mathrm{Li}^+/\mathrm{Li}$.[19] There exist several different types of NMC electrode materials and they vary through variations in the ratio of nickel, manganese and cobalt. Generally, increasing Mn results in increasing safety and cycling life. Increase in Ni improves capacity and C-rate, as well as promising high energy density and voltage of the battery, but demotes in safety. Increase in the amount of Co results in higher achievable C-rates, and higher structural stability,[18,20] see Figure 3. However, even though NMC has the ability to reach high cut-off potentials, generally at voltages above 4.3 V vs. $\mathrm{Li}^+/\mathrm{Li}$, structural degradation of the transition metals starts taking place.[21]

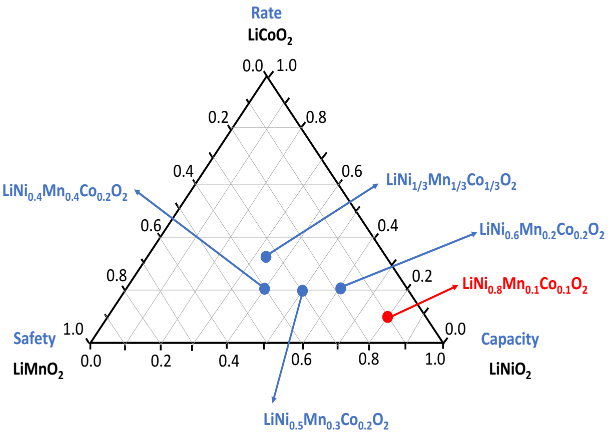

Figure 3. Compositional phase diagram of lithium stoichiometric-layered transition metal oxide: $LiCoO_2$, $LiMnO_2$ and $LiNiO_2$. The positions indicated with blue and red circles describe the $LiNi_{1-x-y}Co_xMn_yO_2$ materials. The most popular NMC-compositions are displayed here. Adapted from[22].

During the last years, more attention has been given to NMC811 as it is considered to have a good compromise between its performance and stability. Furthermore, the use of NMC811, instead of NMC111, reduces the cobalt demand and supply risk for this element. The composition of NMC811 can specifically be written as $Li(Ni_{0.8}Mn_{0.1}Co_{0.1})O_2$. From the description above, this composition results in a stable battery with high capacity, C-rate, energy density and cycling life, which can deliver high voltages.[23]

Graphite is today's established negative electrode material. It features properties as low cost, low potential vs. Li^+/Li, fast diffusion of Li-ions, and relatively small volume changes during intercalation/de-intercalation, as well as having the advantage of high capacity.[24]

2.3 Degradation Mechanisms

As batteries are integrated in several applications, such as in EVs, laptops, and are increasingly used in applications of backup power during power outages, it is necessary to understand how battery usage, also called battery cycling, affects the battery aging.[21] Aging is defined as fade in performance and lifetime.[25] The ambition of research and industry development is to maximize capacity retention throughout the lifetime of the battery, without losing capacity or increasing the resistance. However, due to side reactions, reactions not involved in the energy storing redox reaction, degradation of the battery cell materials occur, eventually leading to cell failure.[21] The effects of repeated cycling, as well as storage, decrease the battery's performance. Capacity decrease and power fading do not either originate from one single cause but from several various processes. Most of these processes cannot be studied independently and occur at similar timescales, complicating the investigation of degradation mechanisms in batteries.

Additionally, the degradation mechanisms occurring at the positive and negative electrodes partially differ.[6]

Battery degradation can be defined in terms of either capacity loss or resistance increase. Capacity loss is an irreversible degradation loss of the ability of a battery to store charge. Resistance increase is defined as an irreversible reduction of the rate at which electrical energy can be accepted or released by the battery.[6] The primary factors causing aging in EV batteries are temperature, voltage and current, all affecting the materials and initiating degradation reactions. Furthermore, the degradation behavior is a part of cell aging.[6]

The overall performance of a cell is influenced by the composition of materials. The rate at which chemical reactions occur in the electrodes and electrolyte, affect the overall performance by affecting the rate of ion diffusion and electron transfer.[6] Aging mechanisms during battery cycling are usually described as the result of degradation of active material and the electrode. This results in an increase in internal resistance, and thereby a decrease in power.[6] Below, Figure 4 illustrates an overview of the common aging mechanisms in LIBs, which are discussed in the following sections.

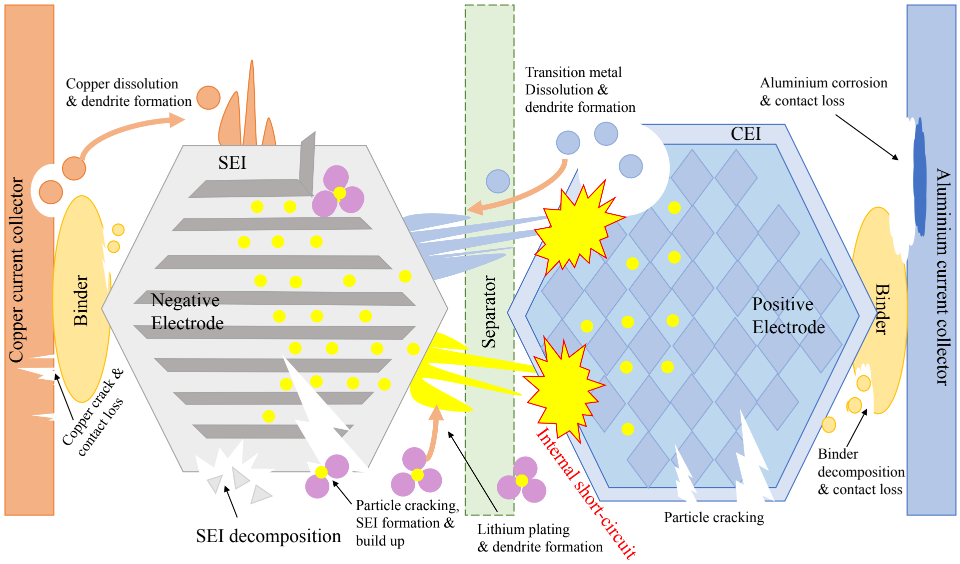

Figure 4. Schematic illustration of aging mechanisms taking place in LIBs. Adapted from[26].

2.4 Degradation Mechanisms at the Negative Electrode

The degradation mechanisms at the negative electrode affect the overall aging behavior in the full battery cell. It is therefore important to understand which mechanisms that initiate degradation in the electrode and why.

2.4.1 Solid Electrolyte Interphase Formation

During the first cycle, also called the formation cycle, a significant decrease in cell capacity is observed. On initial charging, Li-ions diffuse through the electrolyte and are transported to the negative electrode where they are intercalated into the active sites of graphite.[15] Because the electrolyte is not stable at the operating potential of the negative electrode during charging, the electrolyte will react at the negative electrode, forming an interphase layer, called the solid electrolyte interphase, SEI.[28] The chemical composition of the SEI depends on the electrolyte and the electrode used.[6] The SEI is formed as soon as the negative electrode has a low enough potential for electrochemical reactions and should cover the entire negative electrode surface to prevent any further electrolyte decomposition. Once formed, the SEI lays on the surface of the electrode and acts as a phase in the cell. Its main function is to stabilize the interface between the negative electrode and the electrolyte, as well as to inhibit the electron transfer from the electrode surface to the solvent molecules of the electrolyte. Ideally, the SEI is thin, maintaining high ionic conductivity and is electronically insulating. Its physical condition depends on its lifetime and the state of charge of the cell. A battery's state of charge, shortened SoC, defines the battery's current capacity as a function of its rated capacity.[6] The battery capacity, in turn, is determined by the mass of the active material within the battery.[29] During the formation cycle, it is important to charge the cell at a slow rate, in order to form a stable SEI.[6]

Throughout the formation of SEI on the negative graphite electrode, the internal resistance of the battery cell will increase, which hinders the transportation of Li-ions.[21] Throughout the lifetime of a battery, chemical processes contribute to the further formation of SEI. As the thickness of the layer increases, the migration pathway for the Li-ions moving through the SEI also increases, causing a mass transfer resistance which results in a higher internal cell resistance.[30] The degradation processes due to SEI formation generally occur at non-optimal temperatures, or during overcharging of the cell. At high temperatures or during over-charging, the SEI will decompose and crack, causing exposure of the surface of the negative electrode and contributing to further degradation of the electrolyte and Li-ions to form new SEI. The risk of SEI cracking increases throughout the battery cell's lifetime.[30] Furthermore, the properties of the electrolyte may change at low temperatures, subsequently increasing the resistance.[20]

2.4.2 Lithium Plating

Lithium plating is an aging mechanism in LIBs and occurs when Li^+ is reduced at the negative electrode, instead of being intercalated in the active material of the electrode. There are two main reasons for lithium plating. The first reason is due to high currents during charging, causing Li-ions to be transferred at fast reaction rates and therefore accumulate at the surface of the negative electrode. The second reason is charging at low temperatures, resulting in decreasing the reaction rate and affecting the intercalation of Li-ions.[31] This aging process can be avoided by designing battery cells with a higher negative electrode capacity than the positive electrode, enabling the Li-ions to be intercalated into the negative electrode. The long-term effects of lithium plating are an increase in resistance, resulting in a decrease in cell capacity.[21] Lithium plating is typically occurring during cell cycling at low temperatures, in which the low temperatures slows down the Li-ion intercalation into the negative electrode during charging. The Li-ions are therefore deposited on the surface of the electrode, leading to lithium plating.[20]

Furthermore, lithium plating can cause dendrite formation at the negative electrode. If the negative electrode is over-lithiated, lithium will be added at its surface and dendrites will start to be formed, which can puncture the separator, causing a short-circuit in the cell.[21]

2.4.3 Material Degradation

Volume changes in the bulk of the active material during intercalation and de-intercalation lead to mechanical degradation and can cause splits, cracking of the material, and loss of electrical contact, decreasing the Li-ion capacity in the electrode due to loss of active sites. However, the volume changes in graphite are not expected to be more than 10 %. The structural changes may, however, lead to mechanical stress which can result in structural damage and material cracking. Furthermore, there can also occur structural degradation of the material, in which the structure of the active material changes. During intercalation/de-intercalation the active material may undergo phase changes which result in distortion of the crystal lattice. Material degradation can occur at both the positive and negative electrode.[25]

2.5 Degradation Mechanisms at the Positive Electrode

The positive electrode also contributes to the degradation mechanisms of the cell. The degradation mechanisms at the positive electrode generally have a dominant effect during cell operation and especially under harsh conditions, such as during low or elevated temperatures.[32]

2.5.1 Cathode Electrode Interphase Formation

The cathode electrode interphase, *CEI*, formed at the positive electrode is sometimes also referred to as the *SEI at the positive electrode*. This CEI formation is, as the SEI formation, due to side reactions with the electrolyte. These reactions are, however, slower and affect the aging less, in comparison to the SEI formation.[33] Also, the impact from the CEI on the cell performance is lower.[28]

2.5.2 Loss of Active Material and Lithium Inventory

Loss of active material leads to a decrease in capacity and can occur at both electrodes. Several possible degradation mechanisms can cause this, for example, structural transformation of the active material into an inactive phase. Additionally, active material isolation can be caused by, for instance, particle crack formation in the active materials or fracture of the binder.[25] Also, loss of usable Li-ions due to side reactions, such as during the formation of the CEI, leads to loss of lithium inventory.[21]

2.5.3 Transition Metal Dissolution

Transition metal dissolution is a common degradation mechanism in NMC, in which metal ions migrate from the positive electrode, through the CEI, electrolyte, SEI and to the negative electrode, causing capacity decrease, electrolyte decomposition and self-discharge. This results in a resistance increase at both electrodes, and an increase in the amount of side reactions with the electrolyte. The rate at which the metal dissolution occurs depends on parameters such as operating temperatures, potential use, and the composition of the electrolyte.[21] Aging caused by transition metal dissolution is mainly identified in Mn-based positive electrode.[25] Ni-rich positive electrodes do also often suffer from electrochemical degradation, which further causes structural changes at the surface of the active material. During cycling of Ni-rich electrodes, the active materials are known to crack, due to mechanical stress as the cell expands and contracts during cycling. A stable CEI is therefore crucial in Ni-rich electrodes.[34]

2.6 Temperature Dependence

An increase and decrease in the ambient temperature can significantly affect the safety, performance and cycle life of LIBs.[25] During cell operation, the cell performance is strongly dependent on the cell's internal temperature and the ambient temperature. The internal cell temperature will rise due to the nature of the electrochemical redox reactions involved and can be increased as a result of the ambient temperature.[6] The optimal temperature range for LIB is 15–40 °C.[8] Outside this temperature range, the material in LIBs experiences degradation, in which the battery no longer is known to operate under safe conditions. It is important to analyze the effects of low temperatures on LIBs for EVs, to understand how the outdoor temperatures during winter in high-latitude countries may affect these batteries.[9] At low temperatures LIBs cannot be charged safely due to an increase in internal resistance. Lower temperatures inhibit the chemical reactions occurring in the cell, and typical effects are lithium plating and lower ionic conductivity.[35] At temperatures lower than 0 °C, LIBs will show slower chemical reaction activity and decrease in charge transfer rate, which in turn leads to a decrease in ion conductivity in the electrolyte and decrease in Li-ion diffusion between the electrodes. Typically, low temperatures also lead to a significant increase in charge transfer resistance. Earlier studies show that the charge transfer resistance is usually higher for a discharged battery than for a charged one, as it is harder to charge a battery, under these conditions, than to discharge it.[9] The typical processes affected by low-temperature performance in LIB are reduced conductivity of SEI/CEI on the electrode surfaces and increased charge transfer resistance at the electrode–electrolyte interfaces.[36]

There are also several challenges associated with elevated temperatures in LIBs. The major ones include thermal stability of electrodes, separator and electrolyte, as well as reactions within and between these components. Elevated temperatures accelerate structural changes, as well as change properties in the electrolyte and at interfaces such as between the electrodes and electrolyte. There is therefore a big market opportunity for high-temperature batteries that can withstand temperatures of at least 60 °C. This is, however, beyond today's existing technology of liquid electrolytes.[37]

A desired operating temperature for LIBs in EVs is between 80 – 120 °C.[6] However, as, for example, Kabir and Demirocak present,[25] the cycle life of a LIB begins to decline gradually as a result of cell operations at temperatures higher than about 60 °C. The risk for a LIB cell to encounter thermal runaway begins at 70 °C, in which the release in energy causes a further increase in temperature. Efficient thermal management systems can therefore be useful in applications, such as EVs, to keep the temperatures down and still provide a sustainable range. Although there are diverse types of thermal management systems available to keep batteries to working at their ideal temperatures, there remains a need to address issues related to high power consumption, limited temperature range and operation in varying climates.[25] Although cooling systems efficiently extend the temperature limits, safety issues associated with, for example, thermal runaway, cannot be eliminated. Furthermore, thermal management systems become more difficult and critical for larger applications as the surface area per volume of batteries decreases with increased battery size, resulting in a lower heat transfer rate per unit of heat generation. Also, cooling systems result in higher costs and greater weights.[23] Comparing low–temperature effects with high–temperature effects, low–temperature effects are mostly limited to the ambient temperatures, while the effects due to high temperatures happen in a broader range.[32]

2.7 Internal Impedance

Ideally, resistance is the measurement of a circuit element's ability to resist the flow of electrical current, according to Ohms law, and is independent of either AC, alternating current, or DC , direct current. However, most electric loads are reactive and therefore involve both capacitive and inductive components.[19] Unlike resistance, impedance is a frequency–dependent quantity which can be represented by (3). Here, $Z(\omega)$ represents the frequency–dependent internal impedance, $U(\omega)$ the frequency–dependent voltage and $I(\omega)$, the frequency–dependent current.[33] The angular frequency ω is defined by $\omega = 2\pi f$.[40]

$$Z(\omega) = \frac{U(\omega)}{I(\omega)} \tag{3}$$

As electrochemical reactions take place in batteries, electrons and Li-ions are transported through components which have resistive and capacitive characteristics.[41] Ohmic losses are due to the resistance that arises with the flow of electrons through the electrode material, the different interphases, membranes and electrolyte. The ohmic losses result in an increase in internal impedance. Thus, the internal impedance of a battery is desired to be as small as possible.[42]

2.7.1 Electrochemical Impedance Spectroscopy

One main challenge with improving battery efficiency is the inaccessibility to verify battery failure once the battery is built. Electrochemical impedance spectroscopy, EIS, is a popular measurement technique as it provides information about the cell non-destructively. EIS can be used to observe changes in, for example, ohmic resistance, and can further separate and quantify the different impedances within a cell.[6] It is used to study the dynamic characteristics of the electrochemical cells, through measuring the change in electrical impedance as a function of frequency.[6]

EIS is a technique that can measure the resistive, capacitive and inductive components in a battery through applying a sinusoidal voltage $U(\omega)$ and monitoring its current response $I(\omega)$. This type of technique is called potential electrochemical impedance spectroscopy, PEIS, in which the electrical perturbation is a sinusoidal voltage, and the response is a current. Impedance is therefore defined as the resistance that interrupts the current-flow, resulting in a slower current rate, when applying an alternating voltage. The interruptions are represented by circuit elements such as resistors, inductors and capacitors. Essentially, during electrochemical reactions, electrons and Li-ions are transported through battery components in the cell which have resistive and capacitive properties.[41] During a typical EIS measurement, a wide frequency range is selected with a fixed applied voltage amplitude.[40] The frequency range typically depends on the response time of the impedance components, in which slow processes, such as the Li-ion diffusion, are represented at low frequencies (10 Hz to 10 mHz), and fast processes, such as diffusion through the interface layers, are represented at high frequencies (100 kHz to 10 kHz). The common frequency range used for EIS of LIBs is usually 100 kHz to 10 mHz.[41]

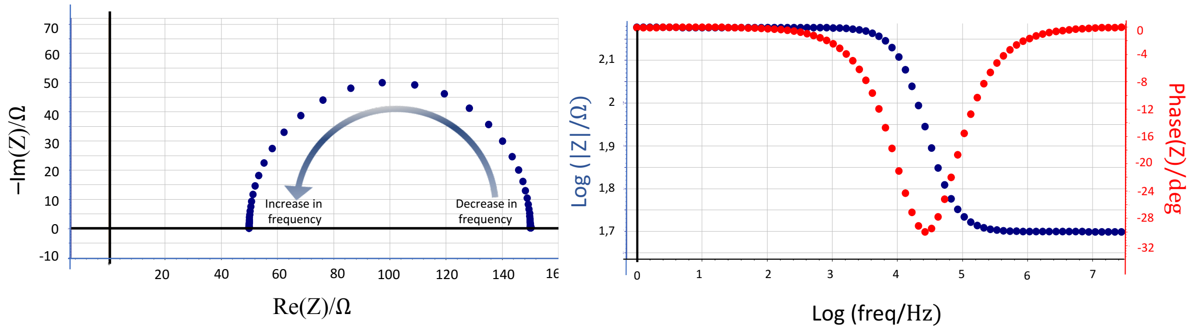

Figure 5. EIS representation by Nyquist plot and Bode plot.

The results from the impedance measurements are usually illustrated in a Nyquist plot or a Bode plot. The Nyquist plot in Figure 5 illustrates the typical impedance semi-circle, in which the high frequencies are measured and plotted to the left, and lower frequencies to the right. On the Nyquist plot, impedance is plotted as a complex number with –Im Z on the y-axis and Re Z on the x-axis. Each plotted point on the Nyquist diagram represents a specific frequency. The characteristic semi-circle displayed derives from a resistor and a capacitor in parallel, and the frequency accounts for the speed at which the various processes take place.[43] The Nyquist plot is a popular graph used for EIS, as its shape yields insights about possible mechanisms occurring inside the battery cell. However, the Nyquist plot does not give any detailed information about the frequency at which the impedance has been measured for each point. Unlike the Nyquist plot, the Bode plot displays the phase angle and the logarithm of the impedance magnitudes on the y-axis and the logarithm of frequency on the x-axis. For more complicated electrochemical systems with several impedance components, the Nyquist plot is often preferred.[41]

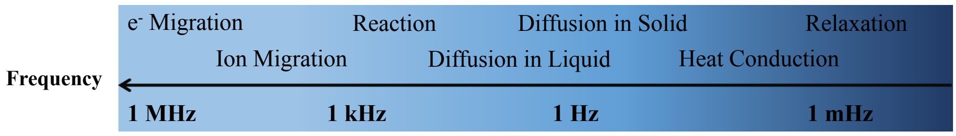

Figure 6. The typical time range for Li-ion time dependent processes in LIBs. Adapted from[17].

As the aging mechanisms of batteries is time-dependent, it is possible to calculate the corresponding time constants for different processes in the battery. The time constants depend, for instance, on the operating conditions, such as temperature. Li-ion diffusion in electrodes is a relatively slow process that corresponds to the time constant for diffusion τ_{diff}, and is calculated according to Table 2, in which x represents the characteristic length of diffusion, and D the diffusion coefficient. The time constant depends on the type of substance the ions are diffusing through, in which diffusion through the electrode, during intercalation and de-intercalation, has a typical time constant of 5 to 20 seconds. Diffusion through substances which change with concentration are heavily dependent on the battery's SoC. Furthermore, the time constant for the transport of charges in solid or electrolyte, are defined by $\tau_{\text{charge,mig}}$. According to this equation, displayed in Table 1, x relates to the characteristic length for conductivity, C_{dl} to the double-layer capacitance at the electrode–electrolyte interface, a_{s} to the specific active area, and κ to the electric or ionic conductivity.[17]

Table 1. The equations for Li-diffusion in LIBs.[17]

Time constants for Li-ion transportation	
Diffusion through electrode	$\tau_{\text{diff}} = \frac{x^2}{D}$
Charge transport in solid and electrolyte	$\tau_{\text{charge,mig}} = \frac{x^2 C_{\text{dl}} a_{\text{s}}}{\kappa}$

The Nyquist plot is usually divided into three main regions, the high-frequency region, the medium-frequency region, and the low-frequency region. These three different regions are briefly described below:

- The high–frequency region (100 kHz–10 kHz): associated with the impedance caused by, the electrolyte, the ionic electrolyte resistance in the separator, and the contact resistances between the current collectors and the electrode plates. The contact resistance describes how well the contact is between electrode particles, electrode and current collector, which may also include the conductivity of the solid particles in the current collectors. The contact resistance is usually described by semi-circular behavior in the Nyquist plot.[44]
- The medium–frequency region (10 kHz–10 Hz): associated with the impedances related to charge transfer reactions.[41] This region is usually represented by a semi-circle, which generally describes the contribution from ion and electron conduction across the thickness of the porous electrode.[44]
- The low–frequency region (10 Hz–10 mHz): represents the impedance effects due to the diffusion of ions across the electrolyte, the electrode–electrolyte interphase.[44] This region demonstrates the slow transportation processes and is usually described with a Warburg element.[41]

The corresponding values for each frequency range can be analyzed through EIS fitting.[41] In order to understand the essential information given by the EIS measurements, it must be fitted into an equivalent circuit model. The equivalent circuit model consists of elements, such as resistors, capacitors, constant phase elements, inductors and Warburg elements.[40]

2.8 Equivalent Circuit Elements

The electrochemical processes in a battery cell that contribute to impedances can in simplified terms be modeled using different circuit elements, as displayed in Figure 7. Since the processes in the positive electrode can have similar time constants, their separate contributions will be convoluted in the impedance spectra. The circuit elements that will be relevant in this study are the resistor, the constant phase element and the Warburg element. Resistors are described according to Table 2. As R is not a function of frequency, through the application of the sinusoidal current in EIS measurements, it only consists of a real component.[40]

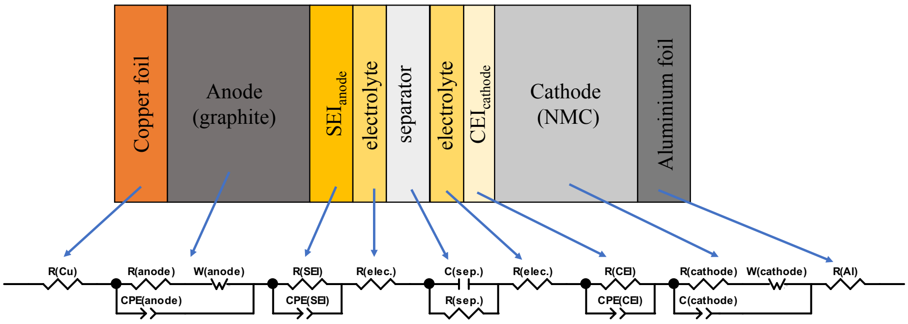

Figure 7. Circuit model and equivalent circuit for the LIB. Adapted from[41].

The impedance of a capacitor increases as the frequency decreases.[40] However, in real systems, there exists some deviation from the ideal behavior that a capacitor has, and therefore this circuit element is referred to as constant phase elements, CPEs. The CPE impedance, Z_{CPE}, is used to account for the non-ideal capacitive behavior due to surface heterogeneities, non-uniform potential and current distributions, and is defined as $\frac{Q}{(\mathrm{j}\omega)^{\beta}}$, in which Q represents the non-ideal capacitance, and β is an ideality factor, ranging between 0 and 1. For $\beta = 1$, $Z_{\text{C}} = Z_{\text{CPE}}$ and $Q = C$.[45]

Table 2. The circuit elements used in the equivalent circuit model.

Equivalent Element	Circuit Model	Formula
Resistor (R)		$Z_{\text{R}} = R$
Constant Phase Element (CPE)	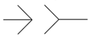	$Z_{\text{CPE}} = \frac{1}{Q(\mathrm{j}\omega)^{\beta}}$
Warburg Diffusion (W)	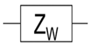	$Z_{\text{W}} = \frac{\sigma\sqrt{2}}{(\mathrm{j}\omega)^{1/2}}$

The inductive impedance is mostly due to the metallic connectors and conducting cables that are connected between the current collectors and the electrochemical analyzers.[45] As this thesis only considers the impedance within a battery, this circuit element will not be considered.

The diffusion of mobile charges, such as the Li-ion diffusion, is described by the Warburg diffusion element, Z_{W}, and is split into two types of diffusions, the finite and infinite diffusion models.[45] The finite-length Warburg impedance, which is associated with the diffusion of charged particles within the electrolyte, and depends on the electrode thickness, is primarily present in the low-frequency region. The infinite diffusion model describes the diffusion through thicker material.[46]

The Warburg finite diffusion model at low frequencies corresponds to the diffusion through thin material and can further be defined as Warburg open and Warburg short.[45] The Warburg open impedance will be of relevance for this project, and is mathematically described by (4).

$$Z_{\mathrm{WO}} = \frac{\sigma\sqrt{2}}{(\mathrm{j}\omega)^{\frac{1}{2}}}\coth\left[\frac{L}{D^{\frac{1}{2}}}(\mathrm{j}\omega)^{\frac{1}{2}}\right] \tag{4}$$

Within the above equations, σ represents the slope gradient and describes resistance related to the diffusion. The terms $L/D^{1/2}$ together represent the lifetime for diffusion, in which L represents the diffusion thickness, and D the diffusion coefficient of a particle.[45]

2.9 Equivalent Circuit Models for Electrode

To understand the data provided by EIS measurements it is necessary to assemble the circuit elements in a physically relevant combination that describes the processes occurring inside the cell, given by the EIS data. There may be several different circuit combinations that provide an equally good fit, and it is therefore important that the circuit fits can be explained logically and physically.[40]

The simplest and most employed equivalent circuit used to model metal oxide electrodes is the *Randles circuit*, see Figure 8 (a), which is used to explain the semi-circle behavior. The circuit is described by the combination of resistances R_1, in series with the parallel elements R_2, and CPE_1. R_1 represents the high-frequency resistances, associated with the resistance of electrolyte, separator, wires, clips and other contacts, while R_2, and CPE_1 in parallel (also denoted R_2/CPE_1) represent the charge transfer resistance of the active material and the electrode–electrolyte interphase. The Randles circuit can be extended with an additional *R/CPE*-combination in series, accounting for a Nyquist diagram with multiple semi-circles. In this thesis, this circuit will be referred to as the *extended Randles circuit*. Each *R/CPE*-combination accounts for a semi-circle observed in the Nyquist plot.[40] In several cases, it is enough to fit data to the Randles circuit, as it can be difficult to distinguish the contributions from different components in the cell; specifically, if the impedance of the diffusion of Li-ions in the electrolyte through the electrode, are of the same order of magnitude. Fitting the impedance spectra to a Randles circuit results in the semi-circle consisting of the sum of the impedances from the contact resistance, the resistance due to the electrode–electrolyte interphase and the charge transfer resistance. Unlike the use of the Randles circuit, fitting impedance spectra through the extended Randles circuit results in two semi-circles, in which the fastest reactions occurring in the cell are observed in the high-frequency semi-circle, and the slower reactions in the low-frequency semi-circle. The high-frequency semi-circle does therefore usually describe the contact impedance, while the low-frequency semi-circle describes the impedance from both the electrolyte interphase and the charge transfer reactions.[46] Furthermore, Figure 8 (b) describes the diffusion of mobile charges through the electrolyte. This circuit is comparable with the Randles circuit, with an additional element of Warburg impedance.[40]

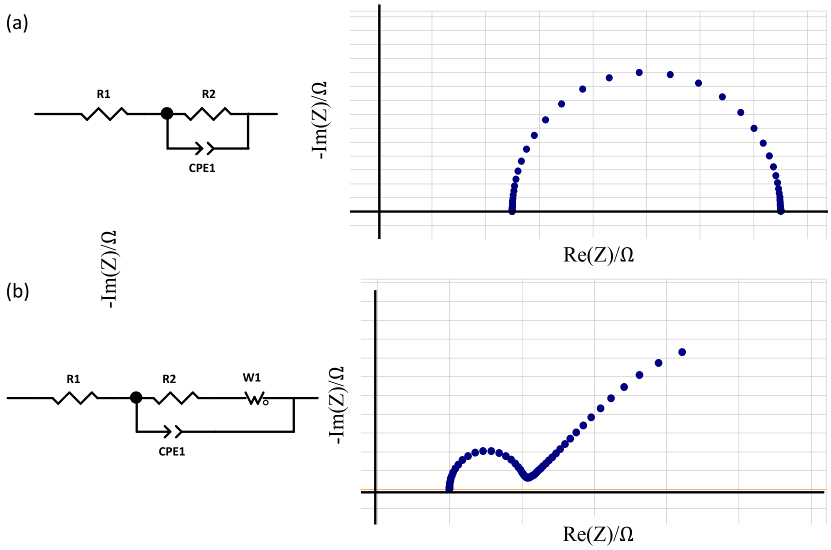

Figure 8. (a) The equivalent circuit and Nyquist diagram for the Randles circuit. (b) The equivalent circuit and Nyquist diagram of Randles circuit, with an additional Warburg impedance.

The last model included in this study is the transmission line model, TLM, pictured in Figure 8 (c). The TLM is a popular way to describe the electrode resistance contribution to the total impedance.[46] The TLM is usually used to describe the impedance response of porous electrodes in LIBs.[47] Compared to other models, such as those described above, the TLM provides additional information about the impedance in the pores of the electrodes.[48] The Randles equivalent circuit treats the electrode as a homogeneous system and does therefore not consider the ionic resistance in the electrode. The TLM is an effective way to analyze the reaction distribution in electrodes with a three-dimensional structure.[49] Elements that influence the internal impedance of the electrode are the electrode and electrolyte interface, and the structural factors of the electrode, such as thickness, composition and porosity. Porous electrodes do mainly undergo four electrochemical processes, described as; (1) conduction with both electron and ion species as electric resistance (R_e), and electrolyte high-frequency resistance (R_{sol}), (2) the formation of an electric double layer at the electrode–electrolyte interface (C_{dl}), (3) the charge transfer reaction for Li-ion intercalation as (R_{CT}), and (4) the mass transfer to compensate for charge as diffusion.[50]

In summary, the resistances of the positive electrode can be described in Figure 9. The high-frequency region describes the resistance of the electrolyte and the ionic electrolyte resistance in the separator. Region I) describes the contact resistance Z_{cont}, between the electrode and the current collector, II) the impedance contribution from ions and electron influences across the electrode Z_{pore}, described with the TLM, or the Randles circuit, and III) the Warburg diffusion impedance Z_{W}.[44]

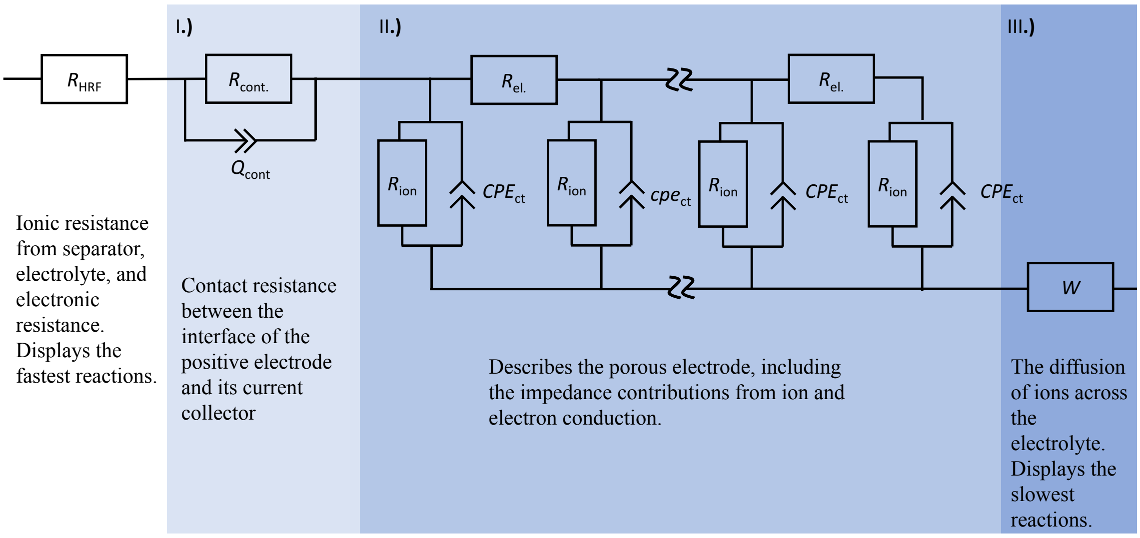

Figure 9. Summary of the different cell impedances for an electrode, in which the pore (II.) is modeled with the TLM. Adapted from[44].

Furthermore, the parallel connection in Figure 9, between $R_{\mathrm{cont.}}$ and $Q_{\mathrm{cont.}}$ is due to the contact resistance between the positive current collector and the positive electrode. The contact resistance is followed by Z_{pore}. The impedance due to Z_{pore}, arises mainly due to the electrode pores, in contact with the electrolyte, forming the electrode–electrolyte interphase. Z_{pore} is composed of the electron resistances R_{el}, describing the electronic resistance inside the solid phase of the electrode. R_{ion} describes the ionic resistance in the electrolyte. Lastly, the charge transfer between the charge transfer reactions between the solid and liquid phase is described by $CPE_{\mathrm{ct.}}$ In general, the electronic resistance in the solid phase is negligible small, in comparison to the R_{ion}.[51] Lastly, Z_{W} is connected in series to Z_{pore}, and describes the salt concentration gradient inside the separator.[44] It is suggested that the intersection of the Nyquist plot with the real axis is mainly represented by the ohmic resistance caused by the electrolyte (R_{sol}).[52]

A simple rule to follow when determining which equivalent circuit model to choose whenever several models have equally good fit, is to select the equivalent circuit with the fewest number of elements that also has physical meaning. For systems which experience some type of change, such as temperature changes, the equivalent circuit with the least changed fitting parameters should be chosen.[46] Furthermore, equivalent circuit modelling can only predict aging processes to a limited extent, mainly because aging processes are associated to a sequence of different aspects.[17] below, is a summary of the different possible aging effects and their consequences in terms of impedance rise.

Table 3. Different aging processes of LIB cells.[20]

Cause	Effect	Enhanced by
Electrolyte decomposition (SEI and CEI formation)	- Loss of Li - Impedance rise	- High temperatures - Overcharging
Gas evolution Cracking formation in particles	- Loss of active material - Loss of Li inventory	- Overcharging - High Ni content in active material
Change in electrode porosity (due to volume changes, SEI/CEI formation and growth)	- Impedance rise	- High cycling rates - High temperature
Contact loss of active material (due to volume changes during cycling)	- Loss of active material - Loss of Li inventory - Decrease in active surface - Impedance rise	- High cycling rates - High temperatures - Overcharging
Decomposition of binder	- Loss of Li inventory - Loss of mechanical stability	- High temperatures
Metallic lithium plating	- Loss of Li inventory - Dendritic growth of metallic Li (can cause short circuit)	- Low temperature - High cycling rate
Transition metal dissolution	- Electrolyte decomposition - Loss of active material	- High and low temperatures - High cycling rates

2.10 Cell Configurations

Four different cell assemblies will be considered in this thesis, according to Figure 10. A full cell is the most common cell arrangement, described above in section 2.1, and displayed in Figure 10. Unlike a full cell, a half cell consists of a positive electrode and a Li-metal electrode. In half cells, the Li-metal electrode works as a reference electrode to facilitate measurements of the cell electrode of interest. The Li-metal is always considered to be the negative electrode, regardless of which positive electrode is used, such as graphite. In this cell arrangement, the negative electrode can provide an infinite supply of Li-ions to the positive electrode, unlike a full cell, which has a limited supply of Li-ions. Half cells are therefore useful when wanting to understand properties separately.[16] For example, the open-circuit voltage can be determined using half cells consisting of lithium metal oxide, or the electrical behavior of the electrode/electrolyte interface.[46]

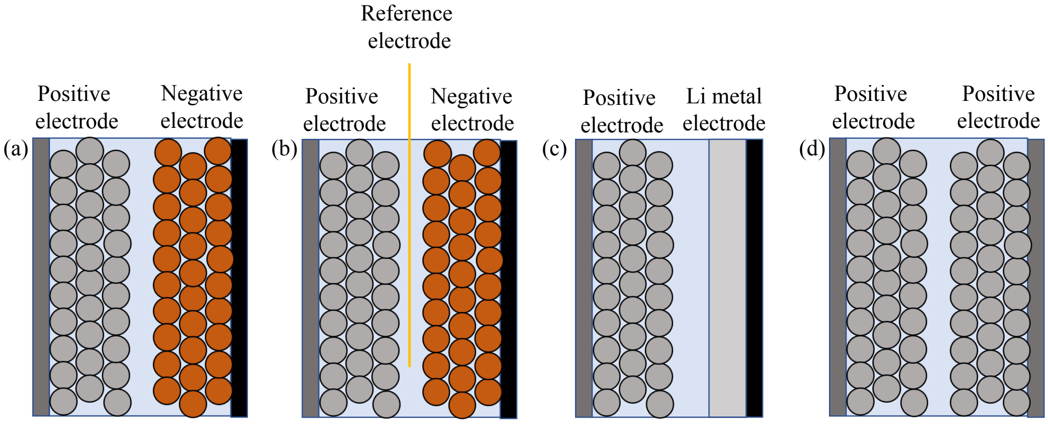

Figure 10. (a) Cell assembly of a full cell, (b) a three-electrode cell with reference electrode, (c) a half cell, and (d) symmetric cell with two positive electrodes. Adapted from[50].

Unlike the assembly of a full-cell, a symmetric cell, Figure 10 (d), consists of two positive electrodes or two negative electrodes. A symmetric cell cannot be charged or discharged, like a full cell, three-electrode cell, or half-cell, but impedance measurements can be completed on the cell as assembled.[52] To analyze the resistance at a different SoC, full cells at a specific SoC can be re-configured into symmetric.[31] Symmetric cells do, however, lack important interactions involving the positive and negative electrode. These cells are often built when wanting to understand the electrochemical behavior between the electrode and electrolyte, more specifically, the internal resistance in the electrode/electrolyte interface. Typically, at a SoC of 0 %, a 45° slope is observed at high frequency which increases in the lower frequency region and eventually forms a vertical line, see Figure 11. The vertical line indicates blocking behavior and suggests the formation of an electrical double layer at the electrode–electrolyte interface, and no charge transfer reactions at the interface, further implicating that the electrode is at an electrochemical equilibrium state and that the resistances which can be interpreted are the high-frequency resistance, electric resistance and ionic resistance. At 50 % SoC a semi-circle appears at lower frequencies, suggesting there is information about ionic resistance and high-frequency resistance in the high–frequency regions and charge-transfer resistance in the lower frequency region.[53]

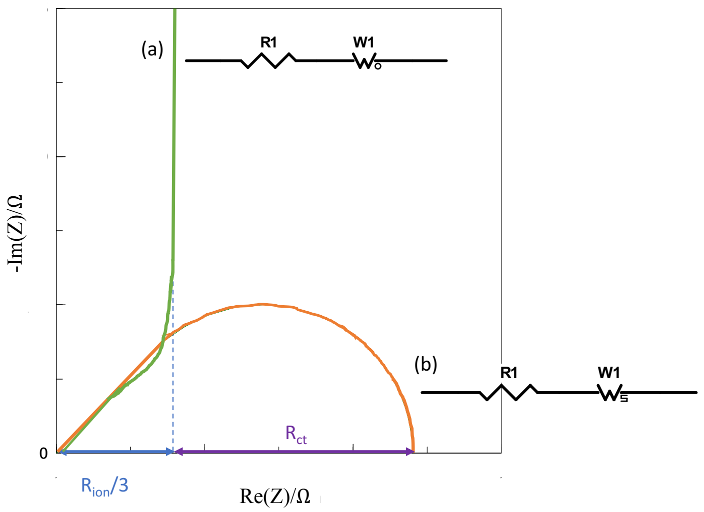

Figure 11. Nyquist plots for symmetric cells using two positive electrodes (LiPF6) at 20 °C. Electrodes were prepared at: (a) SOC = 0 % and, (b) SOC = 50 %. The solid lines are the best-fitted results for the equivalent circuits. Adapted from[53].

In the case of impedance measurements on a positive electrode symmetric cell, the complete cell resistance from the cell is referred to as the double impedance of the positive electrode in a full cell.[43] This is because the impedance spectra of a symmetric cell show the impedance of both the electrodes and the resistance of the electrolyte.[20]

A three-electrode cell consists of a positive, negative and reference electrode, and allows for full cell cycling, at the same time as the reference electrode provides an electrode potential to which the electrode of interest can be referred to. The potential of the reference electrode must therefore be well-defined and stable during the processes of both charging and discharging. Here, as seen in Figure 10 (b), a micro-reference electrode is placed in between the positive and negative electrodes, which allows for an individual determination of the impedance of either the positive or negative electrode.[30] Ideally, the reference electrode is thin, to not interrupt the homogenous current flow between the positive and negative electrodes and without influencing the current flow. The reference electrode must maintain a stable potential regarding time, temperature and should be unaffected by the main electrochemical reactions of interest.[6] There are different metals that can be used as a reference. Li-metal is usually used as a reference electrode in Li-ion cells. However, the potential of the Li-metal reference is not considered to be stable as Li can dissolve due to SEI growth. Furthermore, Cu has also been examined as a reference electrode and is referred to as a reference electrode with long-term potential stability through repeated lithiation, before EIS measurements. Li_3-Au is considered to be stable and the most lithium-rich composition that can be obtained electrochemically.[44]

3. Experimental

In this study NMC811 cells were assembled for cycling and impedance measurements at the temperatures –10, 22, and at 40 ºC.

3.1 Pouch Cell Preparation

Pouch cells were prepared with Al laminate pouch, Cu-metal foil current collector for the negative electrode and Al metal foil for the positive and reference electrode. The Au wire reference electrode, GWRE (core diameter of 0.05 mm and additional 0.007 mm polyimide coating) was used as a reference and connected to the Al current collector, placed in between the positive and negative current collectors. See Figure 12 a) and b). Coating from the last 0.5 cm of one end of the GWRE was partly removed with a scalpel to allow good electrical contact with the current collector. On the other tip of the GWRE, 0.5 mm of the polymer coating was also slightly removed to allow for lithiation of the GWRE, also assuring that the only segment of the wire accessible to the electrolyte was the scratched tip of the GWRE. Sticky tape was used to fasten the current collectors. Two pieces of melting tape were used to seal one side of the pouch cell, and the pouch seal was placed in a sealing machine (*Fermant 400/2*) for a pulse duration of 8.5 seconds with an intensity of 8.5 (arbitrary unit). The pouch cell was thereafter dried in a 60 °C drying oven for at least 22 h, in order for eventual water to evaporate from the pouch cell.

The assembly of the pouch cell was performed in an Argon-filled glove box (< 2 ppm O_2 and < 1 ppm H_2O). During cell assembly, the three-electrode pouch cell was assembled with C as the negative electrode (commercially available graphite electrode coated on Cu-metal foil, from *Customcells*) with a circular diameter of 10 mm, a commercially available positive electrode with a theoretical capacity of 200 mAh/g composed of NMC811 (with 5 % PVDF binder, 5 % conducting carbon super C65, 90 % NMC811, coated on Al-metal foil), punched to a circular diameter of 10 mm, 100 μL of LP40 electrolyte (1 M $LiPF_6$ in 1:1 vol. % of Ethylene carbonate and Diethyl carbonate, from Solvionic), and two separators (Celgard 2325 sheets). No capacity balance was performed between the positive and negative electrodes. The two separators were placed on each side of the GWRE, see Figure 12 b). The theoretical rated capacity was used as a reference for calculation of the C-rates.

To verify the impedance measurements, symmetric cells were built, consisting of two positive electrodes, a separator and half the amount of electrolyte as the three-electrode cells. The current collectors for the symmetric cell consisted of Al. Also, to verify the stability measurements of the gold wire and the positive and negative electrodes, half-cells were built against Li. In the half-cell, the current collectors for the positive electrode consisted of Al-foil, and for the negative electrode Cu-foil was used.

3.2 Cell Cycling and Impedance Measurments

Before lithiation of the GWRE, the pressure of the cells was increased by attaching two 3 mm thick plates on each side of the cell, with help of two clamps. The cells were left at rest for 2 h to allow the separators to get fully wetted by the electrolyte. The GWRE was thereafter lithiated, in which a constant current of –200 nA for 2 h, initially reaching a constant potential of around 0.33 V vs. Li^+/Li. The GWRE was lithiated by applying a current between the positive electrode and the reference electrode, using a multi-channel potentiostat/galvanostat (*Arbin*) instrument. After lithiation, the cell was left for at least one hour at OCV, in which it reached a stable potential of around 0.31 V vs. Li^+/Li.

For the impedance measurement, the three-electrode cell was cycled between 3.0 V and 4.2 V vs. Li^+/Li, with a C-rate of C/5. PEIS was performed by applying a sinusoidal voltage of perturbation amplitude 10 mV, from 100 kHz to 50 mHz. The impedance measurements were obtained at voltages 3.0 V and 3.8 V vs. Li^+/Li, at eight measurements per decade. The cycling protocol was carried out on a potentiostat (*VMP-2*). For experiments carried out at higher temperatures than room temperature, a formation cycle was first carried out at room temperature, 22 ºC, and after completion, the cell was placed in an oven (*Blanc-Lado FN 300*) for cycling and performing impedance measurements at the same voltages. Cells were also assembled for lower–temperature cycling, in which cells were placed in a fridge (*TEFCOLD)* and cycled at –10 ºC. The cycling and PEIS measurements of the cells were obtained at three different temperatures, −10, 22 and 40 °C. At least two cells at each temperature were assembled for three-electrode impedance measurements, to indicate on reproducibility of the impedances spectra obtained.

3.2.1 Fittning data to Equivalent Circuits

The program *ZView* was used for the equivalent circuit fitting of the Nyquist plots and the Bode plot. The equivalent circuit model used was the extended Randles circuit model.

The circuit elements used for the fitting of the equivalent circuit fitting were *R* (resistor), *CPE* (Constant Phase Element) and *W*o (Warburg open). The elements *R*, *CPE* were defined according to Table 2, with the parameters *R* for the resistance. The *CPE* was based on the parameters *CPE-T* (*Q* in the Z_{CPE}-equation), and *CPE-P* defining the exponential factor (β in the Z_{CPE}-equation), in which *CPE-P* = 1 is identical to the capacitor, and *CPE-P* = 0.5 generates a 45 º line in the complex-plane graph, mathematically equivalent to Warburg infinite diffusion,

diffusion through thick material. For the description of a porous surface, usually a CPE-P between 0.9 and 1 is used, due to the double-layer capacitance formed at the electrode–electrolyte interface.

ZView offers both Warburg short and open, with three different parameters, *W-R*, *W-T* and *W-P*. *W-R* refers to the diffusion parameter, *W-T* to the diffusion time of the system in seconds, and *W-P* to the exponential factor, which is fixed to 0.5, according to the equation for Warburg diffusion in Table 2.

The methodological approach for fitting is based on firstly fitting the equivalent circuit models to the Nyquist diagram and the Bode diagram. If the interpretation of the physiochemical phenomena is unreasonable, either a new equivalent circuit model is chosen, or the Nyquist diagram and Bode diagram are fitted by splitting the data into sections and fitting each section to one, two, or three circuit elements.

4. Results and Discussion

The scope of this thesis is to examine the emergence of battery aging, focusing on the positive electrode NMC811. The purpose is to determine how and why increase and fall in temperature affects the aging of NMC811, in terms of the effects on resistance. The study of the positive electrode NMC811's dependence on temperature was done by cycling and measuring the internal impedance of the cell with PEIS at the temperatures –10, 22, and 40 ºC. Furthermore, this thesis only examines the second cycle of each cell. The formation cycle is excluded from the results as the formation of the SEI leads to complicated reactions during the formation cycle.

4.1 Experimental

In this project, the impedance of the commercially available positive electrode material NMC811 was analyzed. The experimental design is based on the Nyquist graphs and voltage profiles from the four different cell configurations presented in section 3.1 and in Figure 10. The objective of the cycling was to obtain impedance measurements at voltages 3.0 V and 3.8 V vs. Li^+/Li, while the cells were cycled between 3.0 V and 4.2 V vs. Li^+/Li, at the three different temperatures. This *Results and Discussion* section refers to the voltage 3.8 V vs. Li^+/Li as both under *charging* or *discharging*. 3.8 V vs. Li^+/Li under charging, refers to the impedance obtained when the cells were charged from 3.0 to 4.2 V vs. Li^+/Li, and impedance measurements were gathered at 3.8 V vs. Li^+/Li. When the cells were discharged from 4.2 V to 3.0 V, impedance measurements were made at 3.8 V vs. Li^+/Li, which is referred to under discharging. Further on, the C-rate vas adjusted, to obtain stable impedance measurements.

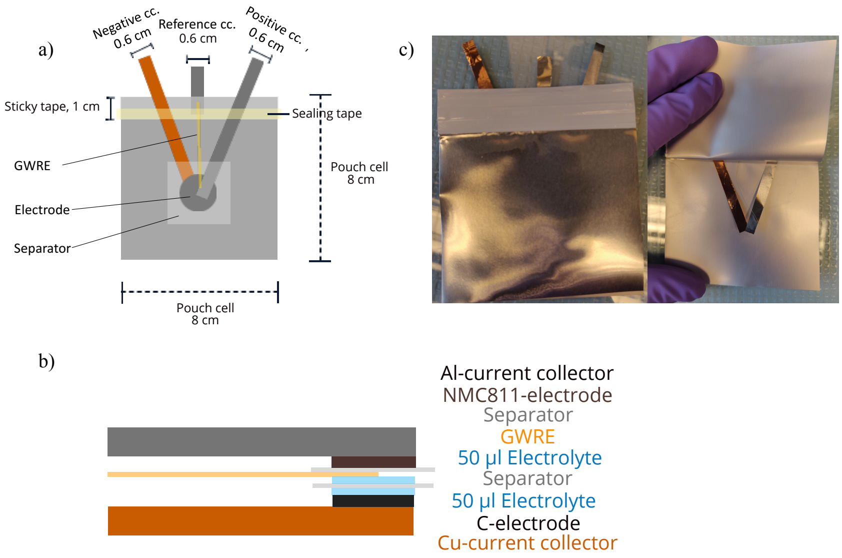

Figure 12. a) Displays the magnitudes and components of a three-electrode pouch cell with a negative current collector (cc.) of Cu-metal foil and the positive and negative current collector of Al-metal foil. b) Side view of (a), in which the pouch bag is not included, but the cc., electrodes, electrolyte and separator are. c) Real-life picture of a three-electrode pouch cell.

To get an indication of the magnitude of the three-electrode cell impedance, symmetric cells consisting of NMC811 were also assembled and impedance measures were obtained at 22 ºC. The impedance for the symmetric cell at 22 ºC, and the impedance of a cycled three-electrode cell at voltage potential 3.0 V vs. Li$^+$/Li, is shown in Figure 13.

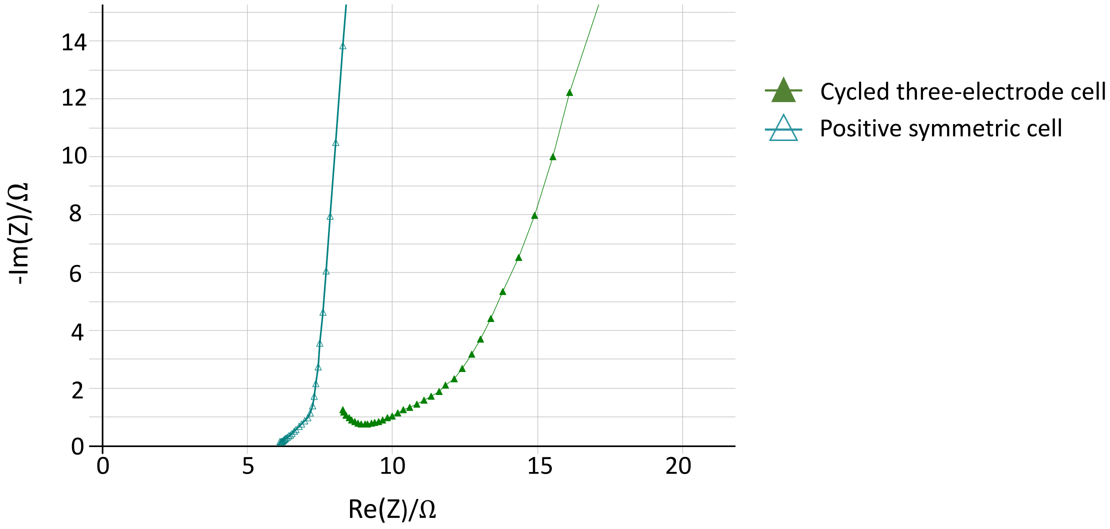

Figure 13. The Nyquist diagrams under blocking conditions display the symmetric cell consisting of NMC811 and the cycled three-electrode cell at 22 ºC, at voltage 3.0 V vs Li$^+$/Li.

When dealing with reference electrodes in an electrochemical system, it is important to define the voltage of the reference. Half-cells, consisting of NMC811, GWRE and Li, were therefore also built to analyze the voltage profile of NMC811 vs. Li^+/Li and NMC vs. the GWRE. Figure 14 displays the voltage profile of the GWRE vs. NMC811, under lithiation.

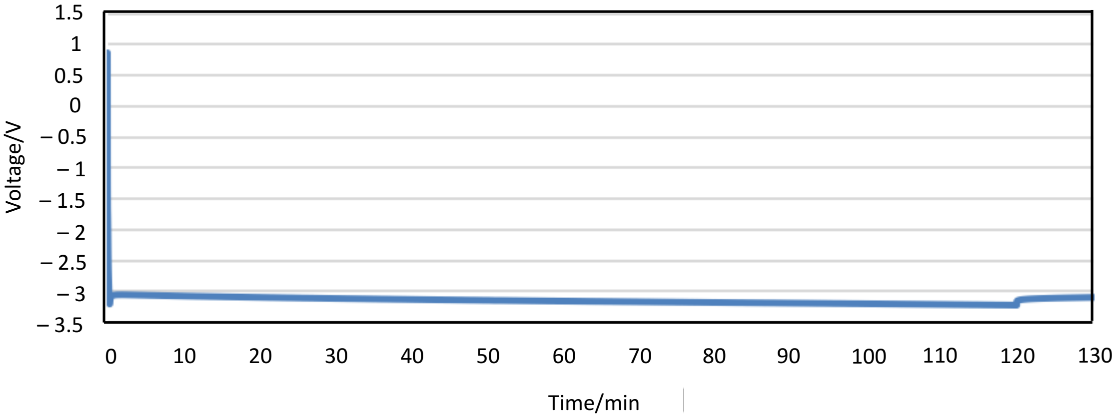

Figure 14. Lithiation of GWRE, vs. NMC811.

The three-electrode cells, cycled at 22 ºC, displayed a stable GWRE which was observed by acquiring stable voltage profiles, similar to the voltage profile in Figure 2, able to achieve several cycles. The cell cycling for the cells at 40 ºC did, however, indicate on an unstable GWRE. This was found as the cell voltage started to fluctuate and increase rapidly, indicating on a drift in voltage for the GWRE. The three-electrode cells, cycled at 40 ºC achieved only one or two cycles, including the formation cycle, before the cells failed. By comparing the voltage profiles of full cells, with three-electrode cells, both cycled at 40 ºC, it was noticed that the full cells accomplished several voltage cycles before being stopped, while the three-electrode cell only achieved one or two cycles, including the formation cycle, indicating that the GWRE had failed. Also, attempts trying to increase the stability of the cycle time of the GWRE were made by completing the formation cycle at 22 ºC, and thereby placing the cell in the oven for the additional cycles. The lithiation of the GWRE was also analyzed by both increasing the lihiation time to 3 and 4 h. However, no increase in the stability time was observed for the three-electrode cell. Moreover, cells were also built and cycled in a freezer at –10 ºC. Stable voltage profiles and impedance measurements were recorded, and the cells achieved several cycles before been stopped.

The use of a GWRE as the reference electrode is built on the studies done by Landesfeind *et al.,* in which impedance measurements at 40 ºC with a GWRE were successfully obtained.[44] Their GWRE was lithiated with a constant current of 150 nA, and cycled at a C-rate of C/2, between 3.0 and 4.9 V, in which the formation cycle was carried out at a C-rate of C/10. They report that by lithiating the GWRE at 25 ºC and then increasing the cell temperature to 40 ºC, the GWRE started to drift to more positive values after less than 10 h, implying an unstable reference. By lithiating the GWRE at 40 ºC, the stability of the reference increased for cycling at the same temperature. Only a small shift in potential by 1–2 mV would be noticed. Furthermore, the authors used another electrolyte (LP57) in their cell assembly. Compared to the procedure carried out for this thesis, the tip of the GWRE was slightly scratched of, in order to enhance the lithiation of the GWRE. To compensate for slightly more accessible Au, than in the Landefseind *et al.* report, the time the GWRE undergoes lithiation is doubled, and the current is higher. The authors also report that a constant potential of 0.31 V vs. Li^+/Li, was yield, which is comparable to the results presented in this report, in which a constant potential of about 0.3 V vs. Li^+/Li was reached. Additionally, the voltage profile and Nyquist diagrams of the three-electrode cells at temperatures –10 and 22 ºC, imply that the GWRE was stable at these temperatures. A suggestion for future studies is that the GWRE should be lithiated at the same temperature as under cycling, to enhance the time of stability, as suggested by Landesfeind *et al.*[44]

4.1.1 Impedance Measurments

The quality of the fitting was measured through the error parameter chi-square ($\mathcal{X}^2$). Chi-square is a good indicator of the fit quality of the chosen circuit model and is used to understand if there is a statically significant difference between expected and observed values. A high chi-square value implies a bad fit and indicates either that an inappropriate equivalent model has been proposed, or inappropriate index data. The size of chi-square can for example be calculated as a function of various SoC, and is estimated by Huang *et al.,* to usually be $<10^{-4}$, based on their data.[54] The estimation can therefore be viewed as a guideline. The fundamental strategy when fitting impedance data is to analyze the association between a small enough chi-square and the physical relevance of the processes occurring in a cell, as chi-square only provides information about how well the model fits the data. At non-blocking conditions, a chi-square of $<10^{-3}$ was obtained. This refers mostly to the cells whose impedance has been captured at voltages 3.8 V vs. Li^+/Li, see Figure 15. For cells under blocking conditions, a chi-square $<10^{-2}$ was obtained. The reason for the differences in order of magnitude of chi-square should depend on the fitting of different equivalent circuits. The Nyquist diagrams of the cells under non-blocking conditions were fitted with the extended Randles circuit. For blocking conditions, the cells were fitted with the equivalent circuit fit of a resistance element and Warburg open in series. The last-mentioned equivalent circuit fit is believed to have a higher chi-square as the low-frequency region was fitted with an exponential factor (W-P) fixed to 0.5, which in the model tends to resemble a vertical. Observing Figure 15 (c), for the Nyquist diagrams at –10 and 22 ºC, it can be noticed that the low-frequency region does not actually approach a vertical line. Therefore, the difference between the observed and expected value increases, and a larger chi-square is obtained.

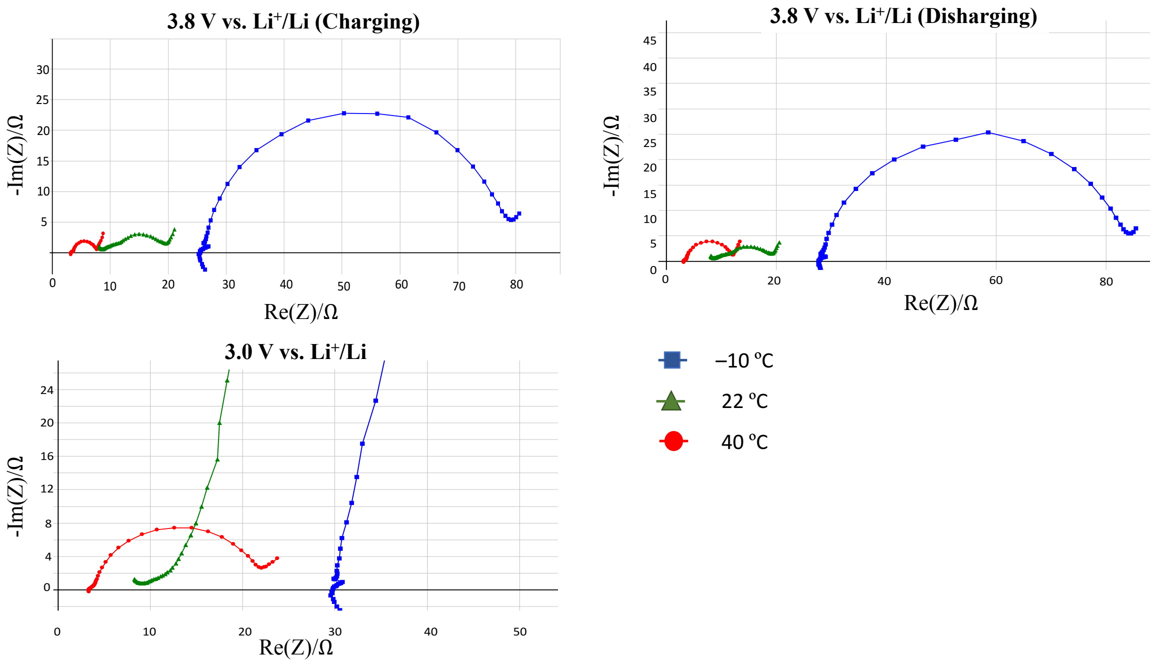

Figure 15. Nyquist plots for the three-electrode cells at –10 ºC, 22 ºC and 40 ºC. Showing the Nyquist plots at: (a) 3.8 V vs. Li^+/Li under charging, (b) 3.8 V vs. Li^+/Li under discharging, and at (c) 3.0 V vs. Li^+/Li.

The equivalent circuit fitting of the cells at 22 ºC was done by fitting the whole Nyquist diagram to the equivalent circuit model and gathering the suggested parameter values from the program. However, this was not possible for the equivalent circuit fitting of the cells at –10 ºC, as the program could not identify the low-frequency semi-circle, see Figure 15. By referring to previous studies and literature, the charge transfer impedance, in the Nyquist diagram referred to as the low-frequency semi-circle, is supposed to be most dependent on temperature, and especially increase at low temperatures. The Nyquist diagram of some of the cells at –10 and 40 ºC were fitted by sectioning the Nyquist diagram and fitting each semi-circle by itself. What is evident from previous studies is that it should be easier to separate the high-frequency semi-circle from the low-frequency semi-circle at lower temperatures than at higher ones. Visually, a small semi-circle can be observed in the high-frequency region, see Figure 15. The reason for the program not being able to identify the high-frequency semi-circle might be explained by the timescale at which the reactions in the high-frequency and low-frequency semi-circles occur,[55] as it seems like these reactions occur at similar time scales.

4.2 Temperature Dependence

In this section, the temperature dependence of the internal resistance of NMC811 is analyzed. The three different temperatures evaluated are –10, 22 and 40 ºC. Figure 15 displays the Nyquist diagram for the second cycle, at these three different temperatures. The impedance measurements were done at 3.8 V vs. Li^+/Li when charging and discharging the cell, as well as at 3.0 V vs. Li^+/Li. The temperature has a significant effect on the impedance, in which it is observed that the impedance at –10 ºC temperatures is significantly larger than for 22 ºC and 40 ºC, for all the figures. Also, a significant shift in the Re(Z)-axis is detected, as the temperature increases. Furthermore, the shape of the Nyquist diagrams presented by Figure 15 at the different temperatures is noticed to differ, depending on the temperature, the SoC and if the cell is charging or discharging.

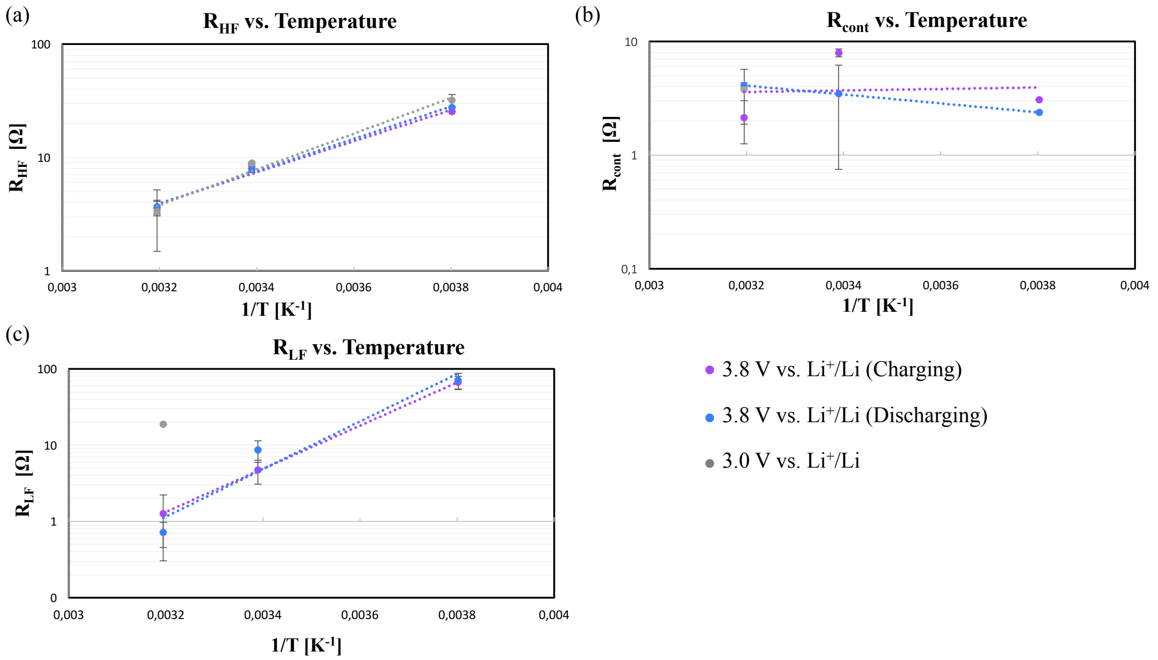

Figure 16. The linear dependence of resistance vs. temperature at temperatures –10, 22 and 40 ºC, and voltages 3.0, 3.8 (charging) and 3.8 (discharging) V vs. Li^+/Li. Note that the exponential function is linear dependent. The datapoints are based on the mean value of two cells for each temperature, except for the high-frequency resistance under charging and discharging at –10 ºC, as well as for the charge transfer resistance at 3.0 V vs. Li^+/Li and 40 ºC. These resistances could only be identified for one cell. However, their Nyquist diagrams are similar. The error bars reflect the minimum and maximum values of the cell's resistances. The slope of the resistances can be used to identify the activation energies of (a) the high-frequency resistance, (b) the contact resistance, and (c) the low-frequency resistance.

As explained in section 2.7.1, the frequency range typically depends on the response time of the impedance components. The fastest processes include the ionic migration through the electrolyte and separator, as well as electron migration in wires and clips. The slower processes include the charge transfer reactions across the thickness of the electrode, and the slowest processes include the diffusion through the electrolyte interphases. As a result of the convolution of the contact resistance, the charge transfer resistance, and the electrolyte interphase resistance, only one apparent semi-circle is observed for each Nyquist plot in Figure 15, expect at –10 ºC, in which two semi-circles are observed. However, by fitting the Nyquist diagrams under non-blocking conditions with the extended Randles circuit, the contact resistance could be extracted. The results are considered on the impedance obtained from two cells at each temperature, which may affect the reliability of the results.

4.2.1 High-frequency Resistance

The high-frequency resistance is often defined as the high-frequency interception with the x-axis, associated with the electric conductivity of the electrolyte in the porous separator. Figure 16 (a) shows the linear dependency between the high-frequency resistance and temperature. It indicates that temperature does have a significant effect on this resistance, in which it is noted that the resistance increases as the temperature decreases. It is expected that the high-frequency resistance increases as a result of an increase in electrolyte resistance.[56] In agreement with literature,[53,55] it can be seen that the high-frequency resistance gradually increases with decreasing temperature. Here, Figure 16 (a), shows that the high-frequency resistance differs between 3.6 and 32 Ω, in between the temperatures –10 ºC and 40 ºC.

Previous studies done by Matsubara *et al.*, show that the CEI formation in Ni-rich electrodes usually involves a thicker CEI than in, for example, NMC111 electrodes.[34] Mainly because the electrolyte–electrode interphase occur faster in these types of electrodes. It has also been presented that the CEI of Ni-rich electrodes, continuously grows under cycling. As electrolyte is consumed under CEI formation, this may explain why the high-frequency resistance is high. At low temperatures, the properties of the electrolyte may change, which results in an increase in resistance, and in this case, an increase in the high-frequency resistance. Furthermore, at low temperatures the ion conductivity of the electrolyte is reduced, which results in an increase in resistance.

Figure 16 (a) shows that the high-frequency resistance has the smallest dependence on the battery's SoC, compared to the other resistances, as similar resistance magnitudes are obtained at each temperature. Regarding the resistance at a voltage of 3.8 V vs. Li^+/Li, it can be noted that the high-frequency resistance during discharge and charging is about the same, which is in agreement with the studies done by Huang, *et al.*[57] Compared to the voltage at 3.0 V vs. Li^+/Li, similar resistance quantities are observed, indicating that the SoC of the high-frequency resistance does not have a significant dependence on temperature.

4.2.2 Contact Resistance

The contact resistance in battery cells refers to the resistance between a current collector and electrode, as well as the conductivity of the solid particles in the electrode. The loss of contact between the active particles in the electrode, and the current collector, leads to an increase in contact resistance. As stated in the background section 2.7.1, the high-frequency semi-circle includes the impedance of the interface between the metallic current collector and the active electrode particles and is considered to be obtained in the high-frequency region. The linear dependency of the contact resistance, displayed in Figure 16 (b), indicates on a weak dependency on temperature, as the regression lines are nearly horizontal. The linear dependency at 3.8 V vs. Li^+/Li under charging is, however, caused by the large variety in resistance, between the different temperatures, as seen in the figure. As the temperature decreases, the contact resistance at 3.8 V vs. Li^+/Li under charging, changes from 2.14, to 7.96 Ω, and further on to 3.08 Ω. Compared to the high-frequency resistance and the low-frequency resistance, the contact resistance is of the smallest change in magnitude, when the temperature is alternated. This indicates that the contact resistance has the smallest dependence on temperature change, which agrees with previous literature, by for example Keefe, *et al.*[55] However, the results presented in Figure 16, regarding the contact resistance suggest that the resistance varies continually depending on the voltage, especially at temperatures 22 and 40 ºC.

Under charging, Li-ions are transported from the positive electrode to the negative electrode. According to Brown's report, regarding Ni-rich NCA, this results in a decrease in the cell volume.[4] During discharging, when the Li-ions are transported back from the negative electrode, the intercalation of Li-ions results in mechanical stress of the active particle, as the cell volume has decreased. In other words, the contact resistance was observed to increase with smaller Li-ion concentration in the active material. Comparing to the results presented here, it is observed that the resistance under charging is higher at temperatures –10 and 22 ºC, during de-intercalation of Li-ions in the active material. It can also be noticed that the resistance magnitude between charging and discharging is higher at 22 ºC than –10 ºC. At low temperatures, reaction rates of the cell occur at a slower speed, which may explain the magnitude difference in contact resistance between charging and discharging at 22 and –10 ºC.

Following Brown's conclusions, the contact resistance for Ni-rich electrodes is expected to increase with a smaller Li-ion concentration in the active material. The contact resistance is therefore expected to be lowest at 3.0 V vs. Li^+/Li, as a higher concentration of intercalated Li is expected to exist in the active material. However, at 40 ºC, the opposite is observed in Figure 16 (b), as the resistance at 3.0 V vs. Li^+/Li is not the lowest. This may, however, not be significant enough, as the resistance magnitudes are within the error bars.

The aging effects that are associated with an increase in the contact resistance are degradation of the binder in the electrode, loss of active material, or due to corrosion of the current collectors. With an increase in temperature, it is noticed that the resistance somewhat decreases, meaning that contact between the positive electrode and the current collector increases. Decreasing the temperature from 40 to 22 ºC causes the contact resistance to increase, in other words, causing loss of contact resistance between the active particles, the electrode and the current collectors.

4.2.3 Low-frequency Resistance

In agreement with several other reports,[53,55,44] the low-frequency semi-circle displays the resistance from both the charge transfer reactions and the electrolyte interphase. This is because of the convolution of the charge transfer resistance and the CEI resistance. The low-frequency semi-circle is represented by an R_{LF}/CPE_{LF} element, in which the R_{LF} element refers to the resistance due to Li-ion insertion at the electrode surface, and the resistance of Li-ion passing through the CEI. The CPE_{LF} elements model the imperfect double-layer capacitance at the electrode–electrolyte interphase, and during the charge transfer reactions. The low-frequency impedance's dependence on temperature can be seen in Figure 15, indicating that the low-frequency semi-circle seems to have the largest dependence on temperature. Figure 16 (c) displays the linear relation between the logarithm charge transfer resistance and temperature, showing that the low-frequency resistance increases exponentially with decreasing temperature. Studies on the low-frequency resistance made by, for example, Liu, *et al.,* suggest that the CEI has a minor variation in resistance, with varying temperature, while the charge transfer resistance increases significantly and rapidly with decreasing temperature.[58] By analyzing the linearity dependence, it can be observed that the low-frequency resistance does indeed have a high dependency on temperature. At –10 ºC, the low-frequency resistance has a magnitude of about 50 Ω, while at 40 ºC the resistance has drastically decreased to be around 1 Ω, during both charging and discharging at 3.8 V vs. Li^+/Li. Furthermore, at 3.0 V vs. Li^+/Li, no low-frequency semi-circles are observed at temperatures –10 and 22 ºC. However, at 40 ºC, a clear low-frequency semi-circle is displayed in Figure 15 (c).

The studies by Ogihara's *et al.*[53] and Keef's *et al.*[55], which both study the charge transfer resistance's dependency on temperature, clarify that this resistance has the most significant dependence on temperature, increasing significantly with a decrease in temperature.[55] The charge transfer resistance ranges from 0.7137 to 54.37 Ω within the temperature range –10 to 40 ºC. The large resistance at low temperatures can be explained by slower chemical reaction rates, which in turn results in a decrease in the charge transfer rate. The charge transfer rate is associated with the ion diffusion between the electrolyte, to the electrode. With a decrease in temperature, this impedance increases as it becomes more difficult for charge transfer reactions to occur at this state. Thereby, it is more difficult to charge a discharged battery at low temperatures. [36]

Furthermore, Zhang *et al*. suggest that impedance increase at low temperatures is associated with the contraction and expansion of the electrode volume, under de-intercalation and intercalation of Li-ions.[36] Under discharge, Li-ions are intercalated to the positive electrode, causing the change of the CEI due to reconstruction of the solid-state interface layer on the electrode surface.[36] As pointed out above, Ni-rich electrodes tend to contribute to higher volume changes during Li-ion intercalation and de-intercalation in the electrode than, for example, NMC111 electrodes. Therefore, the previously mentioned may explain why the charge transfer impedance increases with low temperatures and the resistance due to the formation of the CEI is not expected to change significantly with temperature variations.

With increasing temperatures, the reaction rate increases and the risk for phase transformations at the electrode surface increases. Also, the risk for the decomposition of the electrolyte increases, contributing to further growth of the CEI. The formation of the CEI is, however, known to be a slow process, as explained in the background section 2.7.1. Electrolyte decomposition and high temperatures can in turn cause dried electrodes, increasing the low-frequency impedance.

Figure 15 (c), displays non-blocking conditions at 40 ºC. It can be suggested that this observation is due to the loss of lithium inventory in the electrode. The effects of loss of lithium inventory usually lead to positive potential shifts of both the positive and negative electrode. Hence, at discharge, when the Li-ions have diffused to the positive electrode, the corresponding potential at the positive electrode is at a higher potential. The effect on the cell is enhancing further degradation of active material and cracking of the positive electrode.[59]

Within LIBs, it has been observed that the charge transfer resistance varies significantly with SoC, which also is recognized here. When LIBs are nearly fully discharged, it has been observed that the charge transfer impedance of a nearly fully discharged LIB has a higher impedance than at a higher SoC.[36] However, this is not the case here, in which the impedance for charging and discharging is about the same at al temperatures, within the error bars. The low-frequency resistance observed in Figure 16 (c) increases from 1.3, to 4.7, and further on to 67 Ω, with decreasing temperature, at 3.8 V vs. Li^+/Li (charging). At the same voltage, but under discharging, the resistance increases from 0.7 to 8.9, and further on to 71 Ω, with decreasing temperature.

4.3 Reproducibility and validation

The results are based on two cells at each temperature, in total making it six cells. More cells were constructed for the experimental section. However, due to several factors, such as cell assembly failure, lithiation failure and impedance measurement failure it is believed that the limitation of this study has been based on the stability of the GWRE. On average, two cells at each temperature, indicating similar Nyquist diagrams, voltage profiles and the number of cell cycles, were obtained.

The Nyquist plot of the symmetric cell impedance at 22 ºC, shown in Figure 13, provides information about the interaction between the electrodes and the electrolyte, the resistance due to electron flow and ion diffusion, as well as due to the resistance in the electrolyte. As the Nyquist plots displayed in Figure 13 have been fitted with a R-W_o circuit model, R includes both the resistance in the electrolyte, as well as the contact resistance, while W_o describes the ion diffusion through the electrolyte. However, no charge transfer resistance nor resistance due to the CEI is observed as the cells are at electrochemical equilibrium, and under blocking conditions. What can be seen from the Nyquist plot for the symmetric cell, is that the mean high-frequency resistance is 6.3 Ω, at which the resistance from one electrode is about 3.2 Ω. Figure 13 also displays the Nyquist plot of a cycled three-electrode cell. The cycled three-electrode cell, at 3.0 V vs. Li^+/Li, has a high-frequency resistance of about 8.0 Ω. As explained in the background, section 2.10, the symmetric cell consists of twice the high-frequency resistance of the non-cycled three-electrode cell. However, this implication cannot be observed here, as the resistance from the symmetric cell is 3.2 Ω, and of the three-electrode cell 8.0 Ω. The differences in resistance between these two cells may be explained by the number of separators and amount of electrolyte in the cells, as well as their voltage. The three-electrode cell consists of double the amount of electrolyte and number of separators, in comparison with the symmetric cell. This may explain why the high-frequency resistance is larger for the three-electrode cell than the symmetric cell. Also, the three-electrode cell has gone through cycling, which contributes to the formation of the CEI. The cycled three-electrode cell's impedance has also been measured at 3.0 V vs. Li^+/Li.

The low-frequency region of the Nyquist plots has been fitted with Warburg open, which models the diffusion of Li-ions through the electrolyte. The most likely reason for this region differing for each cell is suggested to be because of the cells being at different potentials and the formation of CEI in the three-electrode cell.

4.3.1 Future work

This thesis has considered the aging mechanisms of NMC811, at temperatures –10, 22 and 40 ºC, at voltages 3.0 and 3.8 V vs. Li^+/Li. It has been indicated that for impedance measurements on three-electrode cells at high temperatures, such as at 40 ºC, it is important to have a stable reference electrode. Although the cells were able to achieve at least two cycles with a stable reference, ideally, a later cycle or cycles would have been preferred. A stable SEI or CEI is not only formed throughout the first cycle but throughout the firsts cycles. Therefore, by analyzing impedance through long-term cycling with PEIS, one could have more insurances that a stable SEI and CEI have been formed. It is also important to remember that equivalent circuit modeling only can predict the aging processes within a battery to a limited extent, mainly because aging processes are associated to a sequence of different aspects.

Furthermore, this thesis has provided some implications about the different aging mechanisms occurring under charge and discharge of a battery by collecting impedance results at 3.8 V vs. Li^+/Li under charging and discharging. As these aging processes depend on time constants, different processes will be magnified at different SoC. By expanding the number of impedance measurements under cycling, an understanding of which aging processes that are magnified at which SoC, could be obtained, and thereby a better understanding of the aging of battery cells. For example, it is in this project difficult to distinguish the difference between the low-frequency impedance and the contact impedance, at –10 ºC. By enhancing the number of impedance measurements under a cycle, the differences between the contact impedance and the low-frequency impedance, under low temperatures, may be evident. Obtaining impedance measurements at several more temperatures, within the same temperature range of –10 and 40 ºC, may also enhance the evidence for cells' temperature dependence, and at which temperature a specific aging mechanism is critical.

To further get an understanding of the impedance within the porous electrodes, the TLM can be used for the analysis. In this study, the TLM is not fitted to the impedance spectra. The focus of this thesis has mainly been on analyzing the general aging trends caused by resistance rise. Fitting impedance spectra with the TLM will give more information about the impedance within the porous electrode. Unlike the TLM, the Randles circuit treats the porous electrode as a homogeneous system and does therefore not include the ionic resistance of the electrode. Therefore, by fitting the impedance spectra with the TLM, one could obtain more information about the aging processes within the porous electrode, and the electrode–electrolyte interphase. Nara *et al*, fitted their impedance spectra with both the Randles circuit and the TLM.[49] They explain that the main differences between the results obtained between these two models were obtaining more impedance values for the aging processes under charging and discharging. Also, the TLM gave insight into the influence of volume changes in the cathode. On the other hand, the values for the charge transfer impedance, R_{ct} and CPE_{ct}, for the TLM were in close accordance to the ones obtained with the Randles circuit.[49] In future studies, the TLM can therefore be used to gain better insight about the aging processes within the porous electrode.

Lastly, in the case of batteries for EVs, it is also important to analyze the influence electrochemical cells have on each other. The impedance analysis of a cell or a component of a cell does not explain enough about how the cell operates in a battery. Also, the results of this project indicate, for instance, that the charge transfer resistance increases with lower temperatures, which might indicate that cell cycling is preferred at higher temperatures. However, this thesis only analyzes the second cycle. As explained previously, the charge transfer reactions occur at a faster rate at high temperatures, in comparison to low temperatures. Suggesting that as reactions occur faster, the material degradation of the cells also occurs at a faster rate. This can be evaluated in further studies by the examination of how internal cell resistance is affected in high and low temperatures, throughout cell cycling.

Conclusion

This thesis had the aim to investigate the degradation mechanisms under cycling of the positive electrode material NMC811. Furthermore, to get an understanding of how and why an increase and decrease in ambient temperature affect the resistance of this battery cell. To establish the temperature dependence of the positive electrode, NMC811, in terms of resistance, PEIS measurements have been investigated at temperatures –10, 22 and 40 ºC. The potentials that have been of interest for impedance measurements were at 3.0 V and at 3.8 V vs. Li^+/Li. The purpose of the thesis has been to develop an understanding of how temperature rise and fall affects the aging of NMC811.

Three-electrode cells were assembled to measure the impedance response of NMC811, which indicated that temperature has a significant impact on resistance. Cell assembly has been demonstrated to be crucial for reproducibility, as it was problematic to assemble and cycle stable three-electrode cells. Nonetheless, impedance measurements were obtained for the three different temperatures and the extended Randles circuit was used for impedance fitting under non-blocking conditions. The resistances which were identified and investigated in this thesis were the resistance associated with the electrolyte and the separator, the contact resistance, the charge transfer resistance, and the resistance due to the formation of the CEI. At –10 and 40 ºC, the charge transfer resistance was observed to have the largest dependency on temperature, in comparison to the four resistances investigated in this thesis. The increase in charge transfer impedance at –10 ºC is suggested to depend on the Ni-rich electrode, which tends to contribute to volume changes in the electrode, affecting the intercalation and de-intercalation of Li-ions. The impedance alternated significantly at 40 ºC, due to the loss of lithium inventory in the active material. The impedance due to contact loss is suggested to have the smallest dependence on temperature, however, significantly affected by the SoC of the cell. The electric conductivity of the electrolyte, separators and electrodes, has on the other hand the smallest dependence on SoC but still a significant dependence on temperature. This thesis has thus shown that temperature has a significant effect on a cell's internal resistances, especially on the electrode–electrolyte interface. For future studies, the TLM can be used to provide more information about the porous electrode.

Reference

(1) 'Progress made in cutting emissions', n.d., in *European Commission*, https://ec.europa.eu/clima/policies/strategies/progress_en. [accessed 9th of July 2020].

(2) 'Transport emission', n.d., in *European Commission*, https://ec.europa.eu/clima/policies/transport_en. [accessed 9th of July 2020].

(3) Saw, Lip Huat, Yonghuang Ye, and Andrew A. O. Tay. 'Integration Issues of Lithium-Ion Battery into Electric Vehicles Battery Pack', *Journal of Cleaner Production,* vol. 113/(2016), pp. 1032-1045.

(4) Brown, S. 'Diagnosis of the Lifetime Performance Degradation of Lithium-Ion Batteries: Focus on Power-Assist Hybrid Electric Vehicle and Low-Earth-Orbit Satellite Applications', Chemical Science and Engineering, Kungliga Tekniska högskolan, Stockholm, (2008).

(5) Korthauer, Reiner, 'Lithium-Ion Batteries: Basics and Applications', Anonymous Translator, Berlin, Heidelberg, Springer Berlin Heidelberg, (2018).

(6) Berg, Helena. *, 'Batteries for Electric Vehicles: Materials and Electrochemistry'*, Anonymous Translator, Cambridge, United Kingdom, Cambridge University Press, (2015).

(7) P. Keil, H. Hesse, S. F. Schuster, R. Arunachala, 'Lifetime Analyses of Lithium-Ion EV Batteries', *ResearchGate,* (2015), .

(8) Genieser, R., S. Ferrari, M. Loveridge, et al. 'Lithium Ion Batteries (NMC/graphite) Cycling at 80 °C: Different Electrolytes and Related Degradation Mechanism', *Journal of Power Sources,* vol. 373/(2018), pp. 172-183.

(9) Ma, Shuai, Modi Jiang, Peng Tao, et al. 'Temperature Effect and Thermal Impact in Lithium-Ion Batteries: A Review', *Progress in Natural Science,* vol. 28/no. 6, (2018), pp. 653-666.

(10) Farjana, Shahjadi Hisan, Nazmul Huda, and M. A. Parvez Mahmud. 'Life Cycle Assessment of Cobalt Extraction Process', *Journal of Sustainable Mining,* vol. 18/no. 3, (2019), pp. 150-161.

(11) A. Dinger, R. Martin, X. Mosquet, M. Rabl, D. Rizoulis, M. Russo, G. Sticher, 'Batteries for Electric Cars - Challenges, Opportunities, and the Outlook to 2020.' *The Boston Consulting Group 2010.*, (2010), .

(12) Amine, Khalil, Ilias Belharouak, Zonghai Chen, et al. 'Nanostructured Anode Material for High-Power Battery System in Electric Vehicles', *Advanced Materials (Weinheim),* vol. 22/no. 28, (2010), pp. 3052-3057.

(13) Xiong, D. 'Surprising Chemistry in Li-ion cells', *Dalhousie University* (2017), .

(14) Whittingham, M. Stanley. 'Lithium Batteries and Cathode Materials', *Chemical Reviews,* vol. 104/no. 10, (2004), pp. 4271-4302.

(15) Palacin, M. R., and A. de Guibert. 'Why do Batteries Fail?', *Science (American Association for the Advancement of Science),* vol. 351/no. 6273, (2016), .

(16) Park, Jung-Ki, and Inc Books24x7. *, 'Principles and Applications of Lithium Secondary Batteries'*, Anonymous Translator(1. Aufl. edn, Weinheim, Wiley-VCH, 2012).

(17) Krewer, Ulrike, Fridolin Röder, Eranda Harinath, et al. 'Review—Dynamic Models of Li-Ion Batteries for Diagnosis and Operation: A Review and Perspective', *Journal of the Electrochemical Society,* vol. 165/no. 16, (2018), pp. A3656-A3673.

(18) 'Comparative Study Nickel Rich Layered Oxides: NMC 622, NMC 811 and NCA Cathode Materials for Lithium Ion Battery', *Meeting Abstracts (Electrochemical Society),* (2018), .

(19) Julien, Christian, Alain Mauger, Karim Zaghib, et al. 'Comparative Issues of Cathode Materials for Li-Ion Batteries', *Inorganics,* vol. 2/no. 1, (2014), pp. 132-154.

(20) Waldmann, Thomas, Marcel Wilka, Michael Kasper, et al. 'Temperature Dependent Ageing Mechanisms in Lithium-Ion Batteries – A Post-Mortem Study', *Journal of Power Sources*, vol. 262/(2014), pp. 129-135.

(21) Björklund, Erik. 'Avoiding Ageing : Surface Degradation of Commercial Electrode Materials in Lithium-Ion Batteries', (2019), .

(22) Liu, Wen, Pilgun Oh, Xien Liu, et al. 'Nickel-Rich Layered Lithium Transition-Metal Oxide for High-Energy Lithium-Ion Batteries', *Angewandte Chemie (International Ed.),* vol. 54/no. 15, (2015), pp. 4440-4457.

(23) Ceylan, Murat, and A. Balikci. 'A Temperature Dependent Model for LTO/NMC

Batteries', *ECS Transactions,* vol. 95/no. 1, (2019), pp. 113-120.

(24) Nitta, Naoki, Feixiang Wu, Jung Tae Lee, et al. 'Li-Ion Battery Materials: Present and Future', *Materials Today (Kidlington, England),* vol. 18/no. 5, (2015), pp. 252-264.

(25) Kabir, M. M., and Dervis Emre Demirocak. 'Degradation Mechanisms in Li-Ion Batteries: A State-of-the-Art Review', *International Journal of Energy Research,* vol. 41/no. 14, (2017), pp. 1963-1986.

(26) Birkl, Christoph R., Matthew R. Roberts, Euan McTurk, et al. 'Degradation Diagnostics for Lithium Ion Cells', *Journal of Power Sources,* vol. 341/(2017), pp. 373-386.

(27) Bruce, P. G. 'Rechargeable Lithium Batteries', *Great Britan* (1996), pp. 1577–1594.

(28) An, Seong Jin, Jianlin Li, Claus Daniel, et al. 'The State of Understanding of the Lithium-Ion-Battery Graphite Solid Electrolyte Interphase (SEI) and its Relationship to Formation Cycling', *Carbon (New York),* vol. 105/no. C, (2016), pp. 52-76.

(29) Moseley, Patrick T., Jürgen Garche, and Peter Adelmann. *, 'Electrochemical Energy Storage for Renewable Sources and Grid Balancing'*, Anonymous Translator(, Amsterdam, Netherlands, Elsevier, 2015;2014;).

(30) Korthauer, Reiner, and SpringerLink (Online service). *, 'Lithium-Ion Batteries: Basics and Applications'*, Anonymous Translator(, Berlin, Heidelberg, Springer Berlin Heidelberg, 2018).

(31) Zinth, Veronika, Christian von Lüders, Michael Hofmann, et al. 'Lithium Plating in Lithium-Ion Batteries at Sub-Ambient Temperatures Investigated by in Situ Neutron Diffraction', *Journal of Power Sources,* vol. 271/(2014), pp. 152-159.

(32) Broussely, M., Ph Biensan, F. Bonhomme, et al. 'Main Aging Mechanisms in Li Ion Batteries', *Journal of Power Sources,* vol. 146/no. 1-2, (2005), pp. 90-96.

(33) Barré, Anthony, Benjamin Deguilhem, Sébastien Grolleau, et al. 'A Review on Lithium-Ion Battery Ageing Mechanisms and Estimations for Automotive Applications', *Journal of Power Sources,* vol. 241/(2013), pp. 680-689.

(34) Takahashi, Ikuma, Hisao Kiuchi, Atsushi Ohma, et al. 'Cathode Electrolyte Interphase Formation and Electrolyte Oxidation Mechanism for Ni-Rich Cathode Materials', *Journal of Physical Chemistry. C,* vol. 124/no. 17, (2020), pp. 9243-9248.

(35) Doughty, D. H.; Roth, E. P. 'A General Discussion of Li Ion Battery Safety', *The Electrochemical Society* (2012).

(36) Zhang, S. S., K. Xu, and T. R. Jow. 'Electrochemical Impedance Study on the Low Temperature of Li-Ion Batteries', *Electrochimica Acta,* vol. 49/no. 7, (2004), pp. 1057–1061.

(37) Lin, Xinrong, Maryam Salari, Leela Mohana Reddy Arava, et al. 'High Temperature Electrical Energy Storage: Advances, Challenges, and Frontiers', *Chemical Society Reviews,* vol. 45/np. 21, (2016), pp.5848-5887.

(38) Basics of Electrochemical Impedance Spectroscopy. Gamry Instruments (2006).

(39) Sihvo, Jussi, Tuomas Messo, Tomi Roinila, et al. 'Online Identification of Internal Impedance of Li-Ion Battery Cell using Ternary-Sequence Injection', *2018 IEEE Energy Conversion Congress and Exposition (ECCE),* (2018), pp. 2705-2711.

(40) A. R. C. Bredar, A. L. Chown, A. R. Burton, B. H. Farnum, 'Electrochemical Impedance Spectroscopy of Metal Oxide Electrodes for Energy Appplications', *Applied Energy Materials* (2020), .

(41) C. Woosung, S. Heon-Cheol, K. Ji Man, C. Jae-Young, Y. Won-Sub, 'Modeling and Applications of Electrochemical Impedance Spectroscopy (EIS) for Lithium-Ion Batteries', *Journal of Electrochemical Science and Technology*, (2019), .

(42) E. Ohuz Koroglu, H. Civelek Yoruklu, A. Demir, B. Ozkaya, 'Microbial Electrochemical Technology - Sustainable Platform for Fuels, Chemicals and Remediation', Elsevier B.V., (2019), .

(43) Ovejas, Victoria, and Angel Cuadras. 'Impedance Characterization of an LCO-NMC/Graphite Cell: Ohmic Conduction, SEI Transport and Charge-Transfer Phenomenon', *Batteries (Basel),* vol. 4/no. 3, (2018), pp. 43.

(44) Landesfeind, Johannes, Daniel Pritzl, and Hubert A. Gasteiger. 'An Analysis Protocol for Three-Electrode Li-Ion Battery Impedance Spectra: Part I. Analysis of a High-Voltage Positive Electrode', *Journal of the Electrochemical Society,* vol. 164/no. 7, (2017), pp. A1773-A1783.

(45) Lvovich, Vadim F. *, 'Impedance Spectroscopy: Applications to Electrochemical and Dielectric Phenomena'*, Anonymous Translator(, Hoboken, N.J, Wiley, 2012;2015;).

(46) Barsoukov, Evgenij, and J. Ross Macdonald. *, 'Impedance Spectroscopy: Theory,*

Experiment, and Applications', Anonymous Translator(2nd edn, Hoboken, N.J, Wiley-Interscience, 2005).

(47) Cruz-Manzo, Samuel, and Paul Greenwood. 'An Impedance Model Based on a Transmission Line Circuit and a Frequency Dispersion Warburg Component for the Study of EIS in Li-Ion Batteries', *Journal of Electroanalytical Chemistry (Lausanne, Switzerland),* vol. 871/(2020), pp. 114305.

(48) Nara, Hiroki, Tokihiko Yokoshima, and Tetsuya Osaka. 'Technology of Electrochemical Impedance Spectroscopy for an Energy-Sustainable Society', *Current Opinion in Electrochemistry,* vol. 20/(2020), pp. 66-77.

(49) Nara, Hiroki, Daikichi Mukoyama, Tokihiko Yokoshima, et al. 'Impedance Analysis with Transmission Line Model for Reaction Distribution in a Pouch Type Lithium-Ion Battery by using Micro Reference Electrode', *Journal of the Electrochemical Society,* vol. 163/no. 3, (2016), pp. A434-A441.

(50) Ogihara, Nobuhiro, Yuichi Itou, Tsuyoshi Sasaki, et al. 'Impedance Spectroscopy Characterization of Porous Electrodes Under Different Electrode Thickness using a Symmetric Cell for High-Performance Lithium-Ion Batteries', *Journal of Physical Chemistry. C,* vol. 119/no. 9, (2015), pp. 4612-4619.

(51) Landesfeind, Johannes, Johannes Hattendorff, Andreas Ehrl, et al. 'Tortuosity Determination of Battery Electrodes and Separators by Impedance Spectroscopy', *Journal of the Electrochemical Society,* vol. 163/no. 7, (2016), pp. A1373-A1387.

(52) Maheshwari, Arpit, Michael Heck, and Massimo Santarelli. 'Cycle Aging Studies of Lithium Nickel Manganese Cobalt Oxide-Based Batteries using Electrochemical Impedance Spectroscopy', *Electrochimica Acta,* vol. 273/(2018), pp. 335-348.

(53) Ogihara, Nobuhiro, Shigehiro Kawauchi, Chikaaki Okuda, et al. 'Theoretical and Experimental Analysis of Porous Electrodes for Lithium-Ion Batteries by Electrochemical Impedance Spectroscopy using a Symmetric Cell', *Journal of the Electrochemical Society,* vol. 159/no. 7, (2012), pp. A1034-A1039.

(54) Huang, Qiu-An, Yue Shen, Yunhui Huang, et al. 'Impedance Characteristics and Diagnoses of Automotive Lithium-Ion Batteries at 7.5% to 93.0% State of Charge', *Electrochimica Acta,* vol. 219/(2016), pp. 751-765.

(55) Keefe, A. S., Samuel Buteau, I. G. Hill, et al. 'Temperature Dependent EIS Studies Separating Charge Transfer Impedance from Contact Impedance in Lithium-Ion Symmetric Cells', *Journal of the Electrochemical Society,* vol. 166/no. 14, (2019), pp. A3272-A3279.

(56) Utsunomiya, Takashi, Osamu Hatozaki, Nobuko Yoshimoto, et al. 'Self-Discharge Behavior and its Temperature Dependence of Carbon Electrodes in Lithium-Ion Batteries', *Journal of Power Sources,* vol. 196/no. 20, (2011), pp. 8598-8603.

(57) Huang, Jun, Jianbo Zhang, Zhe Li, et al. 'Exploring Differences between Charge and Discharge of LiMn2O4/Li Half-Cell with Dynamic Electrochemical Impedance Spectroscopy', *Electrochimica Acta,* vol. 131/(2014), pp. 228-235.

(58) Liu, Xingtao, Zonghai Chen, Chenbin Zhang, et al. 'A Novel Temperature-Compensated Model for Power Li-Ion Batteries with Dual-Particle-Filter State of Charge Estimation', *Applied Energy,* vol. 123/(2014), pp. 263-272.

(59) Gantenbein, Sophia, Michael Schönleber, Michael Weiss, et al. 'Capacity Fade in Lithium-Ion Batteries and Cyclic Aging Over various State-of-Charge Ranges', *Sustainability (Basel, Switzerland),* vol. 11/no. 23, (2019), pp. 6697.

Appendix A – Voltage Profiles

The following figures display the voltage profiles of the second cycle, for the cells discussed in section

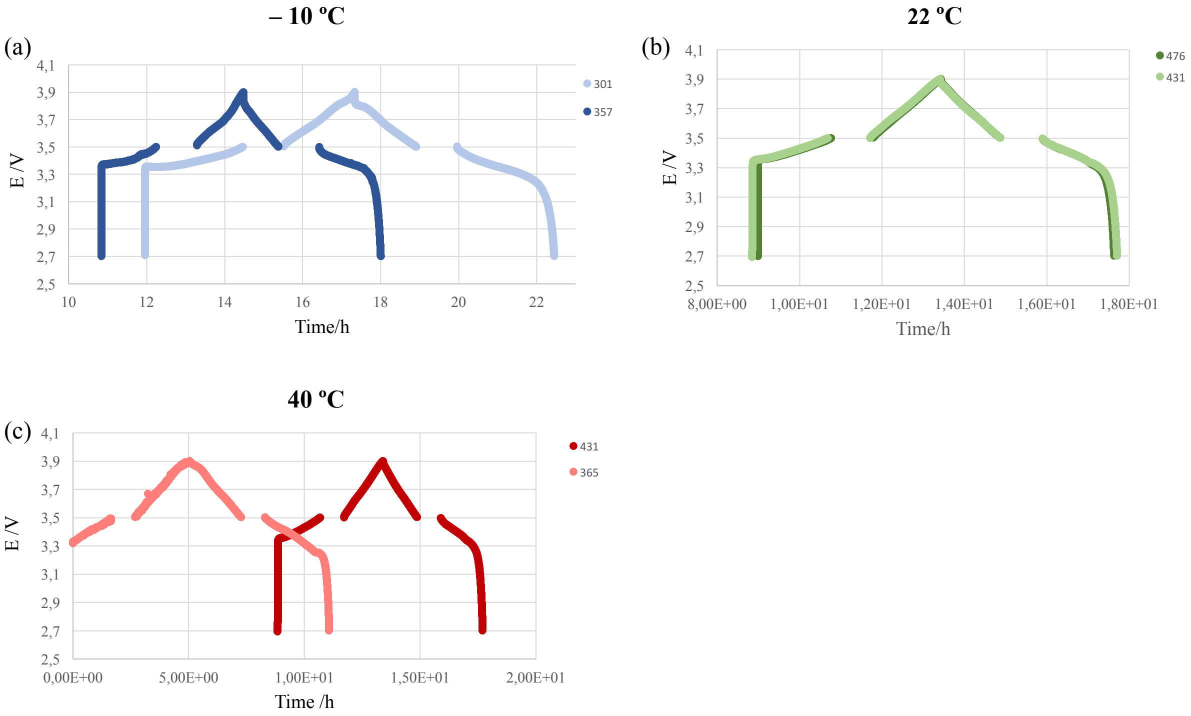

Figure 1. Voltage profile of the second cycle for the cycled cells. The cells are represented by their active masses, shown to the right of the graphs. (a) The voltage profile at –10 ºC, (b) at 22 ºC and, (c) at 40 ºC.

Appendix B – Equivalent circuit data for extended Randles Circuit

The data presented by the fitting program ZView and EC-lab is presented here. The cells are named after their positive electrode, reference electrode and negative electrode, followed by the date the cell was assembled, the positive electrodes active mass and lastly the temperature the cell was cycled at. 10dC refers to –10 ºC. The cycles that are presented and analyzed under section *4. Result and Discussion*. Furthermore, each element is assign a degree of freedom in which + represents a free variable, (+/-) a semi-free element and *X* a fixed element. Lastly, the data table for cell NMC_Au_C_08102020_301_10 dC at voltage 3.0 V vs Li^+/Li, is not presented as reasonable data could not be extracted.

Table 1. Cell NMC811_Au_C_05102020_357_10dC. Impedance measurements taken at voltage 3.8 V vs. Li^+/Li, under charging. As the high-frequency model could not be fitted with the Randles circuit, no values are presented. Here only the second equivalent circuit is presented, which fits the low frequency semi-circle, as well as the Warburg impedance.

Equivalent Circuit	R1+(R2/CPE1)+W_o			
Freedom	Parameter	Value	Error	Error %
+	**R1**	26.83	0.1628	0.6069
+	**R2**	79.83	1.244	1.558
+	**CPE1-T**	0.0009570	0.00001302	1.360
+	**CPE1-P**	0.8451	0.008118	0.9606
+	**W1-R**	0.1152	3.393	2946
+	**W1-T**	0.05166	1.521	1945
X	**W1-P**	0.5	N/A	N/A
	Chi-Square	0.0001575		
	Sum of Square	0.008815		

Table 2. Cell NMC811_Au_C_05102020_357_10dC. Impedance measurements taken at voltage 3.8 V vs. Li^+/Li, under discharging. As the high-frequency model could not be fitted with the Randles circuit, no values are presented. Here only the second equivalent circuit is presented, which fits the low frequency semi-circle, as well as the Warburg impedance.

Equivalent Circuit	R1+(R2/CPE1)+W_o			
Freedom	Parameter	Value	Error	Error %
+	**R1**	34.29	1.856	5.412
+	**R2**	87.46	0.3236	0.3700
+	**CPE1-T**	0.0009842	0.00001054	1.070
+	**CPE1-P**	0.8833	0.003608	0.4085
+	**W1-R**	0.002916	5.756	197410
+	**W1-T**	0.001553	2.066	197410
X	**W1-P**	0.5	N/A	N/A
	Chi-Square	0.0001813		
	Sum of Square	0.008338		

Table 3. Cell NMC811_Au_C_05102020_357_10dC. Impedance measurements taken at voltage 3.0 V vs. Li+/Li.

Equivalent Circuit	R1+ W_o			
Freedom	Parameter	Value	Error	Error %
+	R1	35.91	0.4075	1.135
+	W1-R	22.76	1.695	7.449
+	W1-T	0.007605	0.0006450	8.481
X	W1-P	0.5	N/A	N/A
	Chi-Square	0.002172		
	Sum of Square	0.04996		

Table 4. Cell NMC811_Au_C_08102020_301_10dC. Impedance measurements taken at voltage 3.8 V vs. Li^+/Li, under charging. Here, the first equivalent circuit is used to fit the high-frequency semi-circle, and the other equivalent circuit used to fit the low-frequency semi-circle and the Warburg Impedance.

Equivalent Circuit	R1+(R2/CPE1)			
Freedom	Parameter	Value	Error	Error %
+	R1	24.41	0.08499	0.3345
+	R2	3.08	0.5109	16.58
+	CPE1-T	0.0007986	0.0005061	63.38
+/-	CPE1-P	0.7580	0.07569	9.986
	Chi-Square	0.0006948		
	Sum of Square	0.01390		
Equivalent Circuit	R1+(R2/CPE1)+W_o			
Freedom	Parameter	Value	Error	Error %
+	R1	25.91	0.1359	0.5245
+	R2	53.6	1.38	2.57
+	CPE1-T	0.001204	0.00004473	3.715
+	CPE1-P	0.8987	0.003466	0.3857
+	W1-R	0.3662	4.362	1191
+	W1-T	0.2009	2.393	1191
X	W1-P	0.5	N/A	N/A
	Chi-Square	0.0002558		
	Sum of Square	0.01381		

Table 5. Cell NMC811_Au_C_08102020_301_10dC. Impedance measurements taken at voltage 3.8 V vs. Li^+/Li, under discharging. Here, the first equivalent circuit is used to fit the high-frequency semi-circle, and the other equivalent circuit used to fit the low-frequency semi-circle and the Warburg Impedance.

Equivalent Circuit	R1+(R2/CPE1)			
Freedom	Parameter	Value	Error	Error %
+	R1	27.68	0.05310	0.1918
+	R2	2.37	0.278	11.7
+	CPE1-T	0.0004670	0,0002319	49.67
+/-	CPE1-P	0.8219	0.05826	7.088
	Chi-Square	0.0003136		
	Sum of Square	0.005645		
Equivalent Circuit	R1+(R2/CPE1)+W_o			
Freedom	Parameter	Value	Error	Error %
+	R1	28.0	0.0572	0.204
+	R2	54.4	0.332	0.611
+	CPE1-T	0.001138	0.00001399	1.229
+	CPE1-P	0.9137	0.003626	0.3969
+	W1-R	8.04	1,.30	16.17
+	W1-T	4.914	0.9483	19.29
X	W1-P	0.5	N/A	N/A
	Chi-Square	0.0001738		
	Sum of Square	0.009386		

Table 6. Cell NMC811_Au_C_08102020_301_10dC. Impedance measurements taken at voltage 3.0 V vs. Li^+/Li.

Equivalent Circuit	$R1+W_o$			
Freedom	Parameter	Value	Error	Error %
+	R1	28	0.35	1.3
+	W1-R	8.561	1.077	12.58
+	W1-T	0.004504	0.0006094	13.53
X	W1-P	0.5	N/A	N/A
	Chi-Square	0.001604		
	Sum of Square	0.03047		

Equivalent circuit fitting of cells cycled at 22 ºC

Table 7. Cell NMC811_Au_C_26082020_431_22dC. Impedance measurements taken at voltage 3.8 V vs. Li^+/Li, under charging. The whole Nyquist diagram is fitted to one equivalent circuit.

Equivalent Circuit	$R1+(R2/CPE1)+(R3/CPE2)+W_O$			
Freedom	Parameter	Value	Error	Error %
+	R1	8.606	0.05979	0.6947
+	R2	4.31	0.356	8.25
+	CPE1-T	0.00425	0.000865	20.4
+/-	CPE1-P	0.5357	0.02613	4.878
+	R3	6.35	0.311	4.90
+	CPE2-T	0.00549	0.000158	2.88
+	CPE2-P	0.868	0.0158	2.88
+	W1-R	9.345	1.868	19.99
+	W1-T	12.28	4.371	35.60
X	W1-P	0.5	N/A	N/A
	Chi-Square	0.0001033		
	Sum of Square	0.007124		

Table 8. Cell NMC811_Au_C_26082020_431_22dC. Impedance measurements taken at voltage 3.8 V vs. Li^+/Li, under discharging. The whole Nyquist diagram is fitted to one equivalent circuit.

Equivalent Circuit	R1+(R2/CPE1)+(R3/CPE2)+W_O			
Freedom	Element	Value	Error	Error %
+	R1	8.371	0.06799	0.8122
+	R2	4.10	0.384	9.35
+	CPE1-T	0.004529	0.001103	24.35
+/-	CPE1-P	0.5247	0.03069	5.849
+	R3	5.96	0.326	5.48
+	CPE2-T	0.005665	0.0001889	3.335
+	CPE2-P	0.8749	0.01826	2.087
+	W1-R	9.764	1.676	17.161
+	W1-T	14.09	4.200	29.81
X	W1-P	0.5	N/A	N/A
	Chi-Square	0.0001640		
	Sum of Square	0.01197		

Table 9. Cell NMC811_Au_C_26082020_431_22dC. Impedance measurements taken at voltage 3.0 V vs. Li^+/Li.

Equivalent Circuit	R1+W_o			
Freedom	Element	Value	Error	Error %
+	R1	9.061	0.08450	0.9314
+	W1-R	24.6	1.04	4.22
+	W1-T	0.05042	0.002867	5.686
X	W1-P	0.5	N/A	N/A
	Chi-Square	0.01607		
	Sum of Square	1.173		

Table 10. Cell NMC811_Au_C_24082020_476_22dC. Impedance measurements taken at voltage 3.8 V vs. Li^+/Li, under charging. The whole Nyquist diagram is fitted to one equivalent circuit.

Equivalent Circuit	R1+(R2/CPE1)+(R3/CPE2)+W_O			
Freedom	Element	Value	Error	Error %
+	R1	7.468	0.07977	1.068
+	R2	11.6	0.324	2.79
+	CPE1-T	0.02059	0.002384	11.58
+/-	CPE1-P	0.3267	0.01502	4.597
+	R3	3.08	0.560	18.2
+	CPE2-T	0.006460	0.002044	31.63
+	CPE2-P	1.005	0.03551	3.533
+	W1-R	0.1018	2.969	2917
+	W1-T	0.1102	3.216	2918
X	W1-P	0.5	N/A	N/A
	Chi-Square	0.0000777		
	Sum of Square	0.005674		

Table 11. Cell NMC811_Au_C_24082020_476_22dC. Impedance measurements taken at voltage 3.8 V vs. Li^+/Li, under discharging. The whole Nyquist diagram is fitted to one equivalent circuit.

Equivalent Circuit	R1+(R2/CPE1)+(R3/CPE2)+W_O			
Freedom	Element	Value	Error	Error %
+	R1	7.364	0.1086	1.474
+	R2	2.84	0.704	24.8
+	CPE1-T	0.0068142	0.002841	41.69
+/-	CPE1-P	1.024	0.03786	3.697
+	R3	11.4	0.367	3.21
+	CPE2-T	0.02095	0.002890	13.79
+	CPE2-P	0.3199	0.01846	5.769
+	W1-R	0.09877	3.634	3676
+	W1-T	0.1060	3.898	3676
X	W1-P	0.5	N/A	N/A
	Chi-Square	0.000111		
	Sum of Square	0.007882		

Table 12. Cell NMC811_Au_C_26082020_431_22dC. Impedance measurements taken at voltage 3.0 V vs. Li^+/Li.

Equivalent Circuit	R1+W_o			
Freedom	Element	Value	Error	Error %
+	R1	8.846	0.09946	1.124
+	W1-R	22.3	1.17	5.28
+	W1-T	0.04821	0.003365	6.980
X	W1-P	0.5	N/A	N/A
	Chi-Square	0.02431		
	Sum of Square	1.775		

Equivalent circuit fitting of cells cycled at 40 ºC

Table 13. Cell NMC811_Au_C_03092020_333_40dC. Impedance measurements taken at voltage 3.8 V vs. Li^+/Li, under charging. The whole Nyquist diagram is fitted to one equivalent circuit.

Equivalent Circuit	R1+(R2/CPE1)+(R3/CPE2)+W_O			
Freedom	Element	Value	Error	Error %
+	R1	3.056	0.04889	1.600
+	R2	3.02	0.0863	2.86
+	CPE1-T	0.002726	0.0001045	3.836
+/-	CPE1-P	1.042	0.01193	1.145
+	R3	2.23	0.632	28.4
+	CPE2-T	0.1757	0.04384	24.95
+	CPE2-P	0.2680	0.03671	13.70
+	W1-R	0.7486	0.4495	60.05
+	W1-T	0.7080	0.3712	52.44
X	W1-P	0.5	N/A	N/A
	Chi-Square	0.0003971		
	Sum of Square	0.02978		

Table 14. Cell NMC811_Au_C_03092020_333_40dC. Impedance measurements taken at voltage 3.8 V vs. Li^+/Li, under discharging. The whole Nyquist diagram is fitted to one equivalent circuit.

Equivalent Circuit	$R1+(R2/CPE1)+(R3/CPE2)+W_O$			
Freedom	Element	Value	Error	Error %
+	R1	3.151	0.007765	0.2464
+	R2	7.62	0.03902	0.5124
+	CPE1-T	0.002685	0.00003573	1.331
+/-	CPE1-P	0.803	0.00361	0.369
+	R3	0.456	0.0199	4.36
+	CPE2-T	0.002096	0.0005621	26.81
+	CPE2-P	0.7939	0.03172	3.996
+	W1-R	3.81	0.161	3.22
+	W1-T	2.90	0.175	6.03
X	W1-P	0.5	N/A	N/A
	Chi-Square	0.0001849		
	Sum of Square	0.01460		

Table 15. Cell NMC811_Au_C_03092020_333_40dC. Impedance measurements taken at voltage 3.0 V vs. Li^+/Li. The first equivalent circuit is used to fit the high-frequency semi-circle, and the other equivalent circuit used to fit the low-frequency semi-circle and the Warburg Impedance

Equivalent Circuit	R1+(R2/CPE1)			
Freedom	Element	Value	Error	Error %
+	R1	3.329	0.01576	0.4733
+	R2	0.999	0.397	38.7
+	CPE1-T	0.005153	0.004338	84.18
+/-	CPE1-P	0.6590	0.08419	12.78
	Chi-Square	0.0007852		
	Sum of Square	0.01570		
Equivalent Circuit	R1+(R2/CPE1)+W_o			
Freedom	Element	Value	Error	Error %
+	R1	3.79	0.0602	1.59
+	R2	18.7	0.607	3.25
+	CPE1-T	0.003671	0.0002006	5.465
+	CPE1-P	0.8655	0.004202	0.4855
+	W1-R	0.1612	1.95	1209
+	W1-T	0.13	1.57	1209
X	W1-P	0.5	N/A	N/A
	Chi-Square	0.0003652		
	Sum of Square	0.01753		

Table 16. Cell NMC811_Au_C_21092020_365_40dC. Impedance measurements taken at voltage 3.8 V vs. Li$^+$/Li, under charging. The whole Nyquist diagram is fitted to one equivalent circuit.

Equivalent Circuit	R1+(R2/CPE1)+(R3/CPE2)+W_O			
Freedom	Element	Value	Error	Error %
+	R1	4.095	0.01717	0.4192
+	R2	1.26	0.103	8.179
+	CPE1-T	0.02305	0.005797	25.15
+/-	CPE1-P	0.4191	0.02037	4.861
+	R3	0.305	0.198	64.1
+	CPE2-T	0.001847	0.001618	87.61
+	CPE2-P	1.065	0.04828	4.533
+	W1-R	0.003035	0.8972	29565
+	W1-T	0.003791	1.121	29566
X	W1-P	0.5	N/A	N/A
	Chi-Square	0.0001461		
	Sum of Square	0.01037		

Table 17. Cell NMC811_Au_C_21092020_365_40dC. Impedance measurements taken at voltage 3.8 V vs. Li^+/Li, under discharging. The whole Nyquist diagram is fitted to one equivalent circuit.

Equivalent Circuit	R1+(R2/CPE1)+(R3/CPE2)+W_O			
Freedom	Element	Value	Error	Error %
+	R1	4.199	0.01459	0.3474
+	R2	0.5513	0.04726	8.572
+	CPE1-T	0.001859	0.0007315	39.36
+/-	CPE1-P	0.6520	0.03980	6.104
+	R3	0.9719	0.03762	3.871
+	CPE2-T	0.002761	0.0001540	5.579
+	CPE2-P	0.8761	0.01453	1.659
+	W1-R	0.5100	0.03199	6.273
+	W1-T	0.6791	0.06304	9.283
X	W1-P	0.5	N/A	N/A
	Chi-Square	0.0001030		
	Sum of Square	0.007512		

Equivalent circuit fitting of symmetric cells at 22 ºC

Table 18. Symmetric cell NMC811_NMC811_28072020_1_22dC. Impedance measurements at blocking conditions.

Equivalent Circuit	R1+W_O			
Freedom	Element	Value	Error	Error %
+	R1	6.617	0.01455	0.2199
+	W1-R	5.459	0.1006	1.843
+	W1-T	0.002709	0.00006263	2.312
X	W1-P	0.5	N/A	N/A
	Chi-Square	0.0008274		
	Sum of Square	0.04220		

Table 19. Symmetric cell NMC811_NMC811_03082020_2_22dC. Impedance measurements at blocking conditions.

Equivalent Circuit	$R1+W_O$			
Freedom	Element	Value	Error	Error %
+	R1	6.047	0.01314	0.2174
+	W1-R	4.169	0.07903	1.896
+	W1-T	0.002070	0.00004564	2.205
X	W1-P	0.5	N/A	N/A
	Chi-Square	0.0006011		
	Sum of Square	0.02825		